Report on model of potential drill target and proposed drill path

Work Package 7

Deliverable – D7.1

Report on model of potential drill target and proposed drill path

Work Package 7

Deliverable – D7.1

Elisabeth Peters (TNO, Utrecht), Thibault Candela (TNO, Utrecht), Baptiste Lepillier (TUDelft, Delft), Hannes Hofmann (GFZ, Potsdam), Paromita Deb (RWTH, Aachen), Michal Kruszewski (Fraunhofer IEG, Bochum), Walter Wheeler, Eivind Bastesen (Norce, Bergen), Eugenio Trumpy (CNR, Pisa), Leandra Weydt, Kristian Bär, Ingo Sass (TUDA, Darmstadt), Jan Diederik van Wees (UU, Utrecht)

Version: final

Work package 7

29 June 2020

Website: http://www.gemex-h2020.eu

The GEMex project is supported by the European Union's Horizon 2020 programme for Research and Innovation under grant agreement No 727550 and the Mexican Energy Sustainability Fund CONACYT-SENER, project 2015-04-268074

Table of Contents

List of figures

List of tables

Executive summary

Within the GEMex project, the potential for Enhanced Geothermal System (EGS) development at the site of Acoculco (Mexico) has been investigated. At the site, two exploration wells were drilled in the past, which showed high temperature (~300 °C at 2 km depth) but very low permeability. In this report, the production is estimated for EGS stimulation concepts from GEMex task 7.2 which are reported in deliverable 7.2. The stimulation concepts were translated into field development scenarios using different assumptions on how the stimulation might affect the permeability in the subsurface. In total, 12 scenarios were identified based on 4 different stimulation concepts for 3 depths each. The stimulation concepts are: hydraulic fracture (tensile), stimulated fracture network, stimulated fault (shear) and a combination of stimulated fractures and a fault. The three depths used are 800 m, 1500 m and 1800 m. The most shallow depth is most likely to be stimulated in case of open hole stimulation. At 1500 m, the target might be (fractured) marbles which could be stimulated and at 1800 m, the contact zone between the skarn and the granites could be the target.

For these scenarios, production was simulated for 20 years and the resulting heat production analysed. For all the hydraulic fracture scenarios, premature cold water breakthrough was an issue. In these scenarios, the stimulated rock volume is too small to sustain the temperature for more than a few years. In the scenarios in which it was assumed that a connected fracture network was stimulated, heat production is much better. A main question is if such a network of fractures is present. In case a fault is stimulated, also the stimulated volume is estimated to be much larger than for a hydraulic fracture and thermal breakthrough is delayed. The achieved width of the stimulated fault zone has a large impact on the production. If the fault intersection with the well is limited, the required drawdown for inflow into the well can be considerable, which also negatively impacts the heat production. The combination scenario can also give good heat production, provided the cross flow across the fault is assumed. Whether this is realistic depends on the fault architecture.

For each scenario, uncertainty about the stimulation results was incorporated by simulation of 50 realizations rather than one. To parametrize the realizations, the values for the size and permeability of the stimulated area were sampled from a probability distribution. Other uncertainties were not included in the analysis. This limited uncertainty analysis already gave a large spread in cold water breakthrough and produced heat

The analysis of induced seismicity demonstrates for both the strike-slip fault model and normal-slip fault model, that induced thermoelastic stress changes can lead to a high relative rate of induced seismicity ($R>10^4$, where R is the relative increase in natural seismicity rate). A clear risk of induced seismicity by cooling of the pre-existing faults is identified in this study, given the assumption made in this study. Our analysis predicts a higher level of induced Coulomb stress and induced seismicity for the normal-slip fault model than for the strike-slip fault model. The number of events at each magnitude is expected to be higher for the normal-slip fault model than for the strike-slip fault model.

1 Introduction

1.1 Concept of EGS systems

The goal of work package 7 of GEMex is to design and evaluate concepts for the development of an Enhanced Geothermal System (EGS) at Acoculco. Different definitions and interpretations of EGS have been given (e.g. Olaso et al., 2016, Calcagno et al., 2010 from the ENGINE project), but central is that heat is extracted from the subsurface via an enhanced or engineered system and not from a natural hydrothermal system. In general in EGS the natural permeability is too low to allow for economical production without extensive stimulation. The stimulation takes the form of fracturing, either through hydraulic means by injected water/fluids/CO_2 under high pressure or cold water/fluids/CO_2. In this way natural fractures or faults are stimulated and/or fractures are created. The concepts and the stimulation techniques applied should be capable of achieving sufficiently high and sustainable flow rates, in such a way that environmental effects are minor and acceptable.

To realize sufficiently high and sustainable flow rates or more generally economically producible amounts of heat, a sufficiently large volume of rock should be accessible for heat transfer (Sanyal, 2010; Grant, 2016; Blöcher et al., 2016). The volume of the stimulated rock should be in the order of 0.1-0.3 km^3 (Jung 2013). In general this requires either stimulation of a natural fracture system, or the creation of multiple fractures (Hofmann et al., 2014). Achieving economic total flow rates from an EGS system may require producing from more than one stimulated volume (Doe et al., 2014).

One of the main environmental effects of creating and using EGS systems, is the potential for induced seismicity. In traditional hydraulic stimulation, water with proppants is injected at high pressure and mode I, tensile fractures are created, which are kept open with proppants (e.g. Miskimins, 2019). For the development of EGS, in general also water is injected at high pressure, but mostly below fracturing pressure; permeability is created via shear (mode II) fracturing of mostly pre-existing faults/fractures planes. The stimulated fractures are assumed to stay open due to the natural surface roughness, also called the self-propping effect (Courson and Cowan, 1980; Zimmermann et al., 2010). In practice, during stimulation both modes of rock failure may occur (McClure and Horne, 2014). Shearing along fractures or fault planes can induce seismic events, which are generally small but can be larger depending on the stress state, depth and fault architecture (Evans et al., 2012; Buijze et al., 2019). During the operation of an EGS system, the injection of large amounts of cold water creates additional risks for induced seismicity (Buijze et al., 2019).

1.2 Workflow for EGS concept development

Development of an EGS is complex and technologically demanding, which is the result of a combination of generally large uncertainty in subsurface characteristics with technology that is still under development. Integral parts of a workflow for EGS development should therefore be risk management and uncertainty analysis (Witter et al 2019). During the first phase of exploration, often a recovery factor is used to estimated the geothermal potential of a site (e.g. Swyer et al., 2018). As more information becomes available, production or field development scenarios can be created and simulated to improve upon the geothermal potential estimate based on a recovery factor only. Eventually this should result in information which can be used to support a decision whether to develop a site and how to develop it (Bickel and Bratvold, 2008).

In Figure 1-1 the workflow is illustrated to arrive at development scenarios. In the first step, the site should be characterized, addressing the main aspects of the site that determine its potential for EGS development:

- Characterization of the heat source

- Subsurface characterization (faults, fractures, formations, in situ stress)
- Petrophysical and rock mechanical characterization of the target formations
- Hydrogeological characterization (less relevant for Hot Dry Rock (HDR))
- Geochemical characterization

The characterisation of Acoculco has been addressed in WPs 3 to 6 of the GEMex project and has been reported in a range of deliverables. In the second step, concepts are developed about how an EGS can be created given the characteristics of the site. These are captured in EGS stimulation concepts. Based on these concepts, field development scenarios are formulated. In the final step, numerical models are used to evaluate the potential production of the different field development scenarios. The numerical model approaches used at this stage of development (i.e. exploration phase) are generally relatively simple and fast to allow a stochastic approach (e.g. Quinao and Zarrouk, 2018). A stochastic approach is preferred, to allow for incorporation and quantification of the uncertainty. The site characterization from the first step is used to parametrize the numerical simulation models for both the stimulation and the production evaluation. For a complete evaluation of a potential EGS development also safety aspects such as induced seismicity and environmental risks and social acceptance should be evaluated. All aspects are addressed in WP7 of the GEMex project. Below is an overview of the four interrelated deliverables of WP7:

- D7.1 (this report): Estimation of production performance and induced seismicity during production for the development scenarios based on the stimulation concepts from D7.2.
- D7.2 (Hofmann et al., 2020): Evaluation of stimulation options for Acoculco, resulting in concepts for EGS stimulation in Acoculco. Also induced seismicity during stimulation is addressed.
- D7.3 (Peters et al., 2020): This report focuses on environmental impact. It summarizes risks of induced seismicity and gives recommendations for passive micro-seismic monitoring and traffic light systems. Also, chemical hazards and base line monitoring are described.
- Public engagement and conceptual models on how to engage the local communities are discussed in D7.4 (Contini (eds.), 2020).

This report only discusses production performance for different development scenarios including the drill targets. The design of well completions and surface facilities will not be addressed here. Cost estimates are also not included

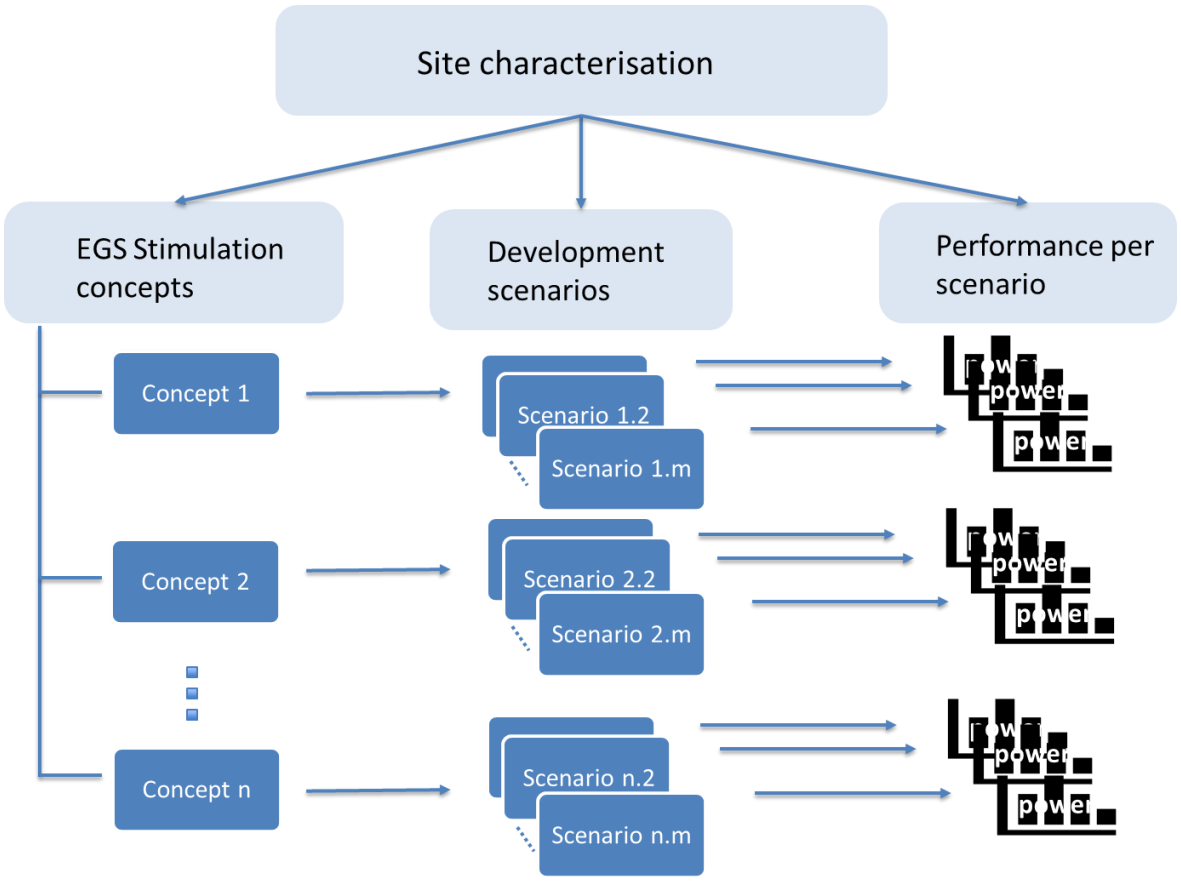

Figure 1-1. Illustration of the workflow to estimate performance including uncertainty of the potential EGS development at Acoculco.

1.3 Setup of the report

In this report, first (Chapter 2) the Acoculco area will be described. To avoid duplication with other deliverables, the focus is on the information that is most relevant for the development of an EGS. In Chapter 3, the field development scenarios are presented. In this chapter, also the translation of the conceptual scenarios to numerical models is described. Finally, the parametrization of the numerical simulation models is discussed. In Chapter 4, the results are presented in terms of key performance criteria at both downhole and surface conditions. The induced stresses and induced seismicity that could be caused during production are discussed in Chapter 5. Final conclusions are presented in Chapter 6.

2 Site description of Acoculco

2.1 Description of the area

The Acoculco Caldera is generally characterised as a Hot Dry Rock (HDR): a very tight reservoir with low fluid content which needs to be stimulated in order for the heat to be producible (e.g Gupta and Roy, 2007). The site has been identified as a potential EGS already in the 1980s and the first exploration well EAC-1 was drilled in 1995 (López-Hernández et al., 2009). The well found temperatures of up to 300°C at 2000 m depth, but was also very tight. The temperature profile was consistent with conductive thermal conditions.

During drilling some minor fluid losses were observed at three depths (1369 m AH, 1736 mMD and around 1910 mMD) (Kruszewski et al., 2020 in review), but flow testing showed poor permeability at the potential reservoir depth (> 1000 m). The temperature profile in EAC-1 indicated some zones with possible convection at depths of 1250 and 1650 m MD (Lorenzo Pulido et al., 2010), which were not consistent with the fluid losses. In 2008 a second well, EAC-2 was drilled which found similar conditions (Kruszewski et al., 2020 in review). The interpretation of the stratigraphy in the wells was updated in the GEMex project (González Partida, 2019) and is illustrated in Figure 2-1.

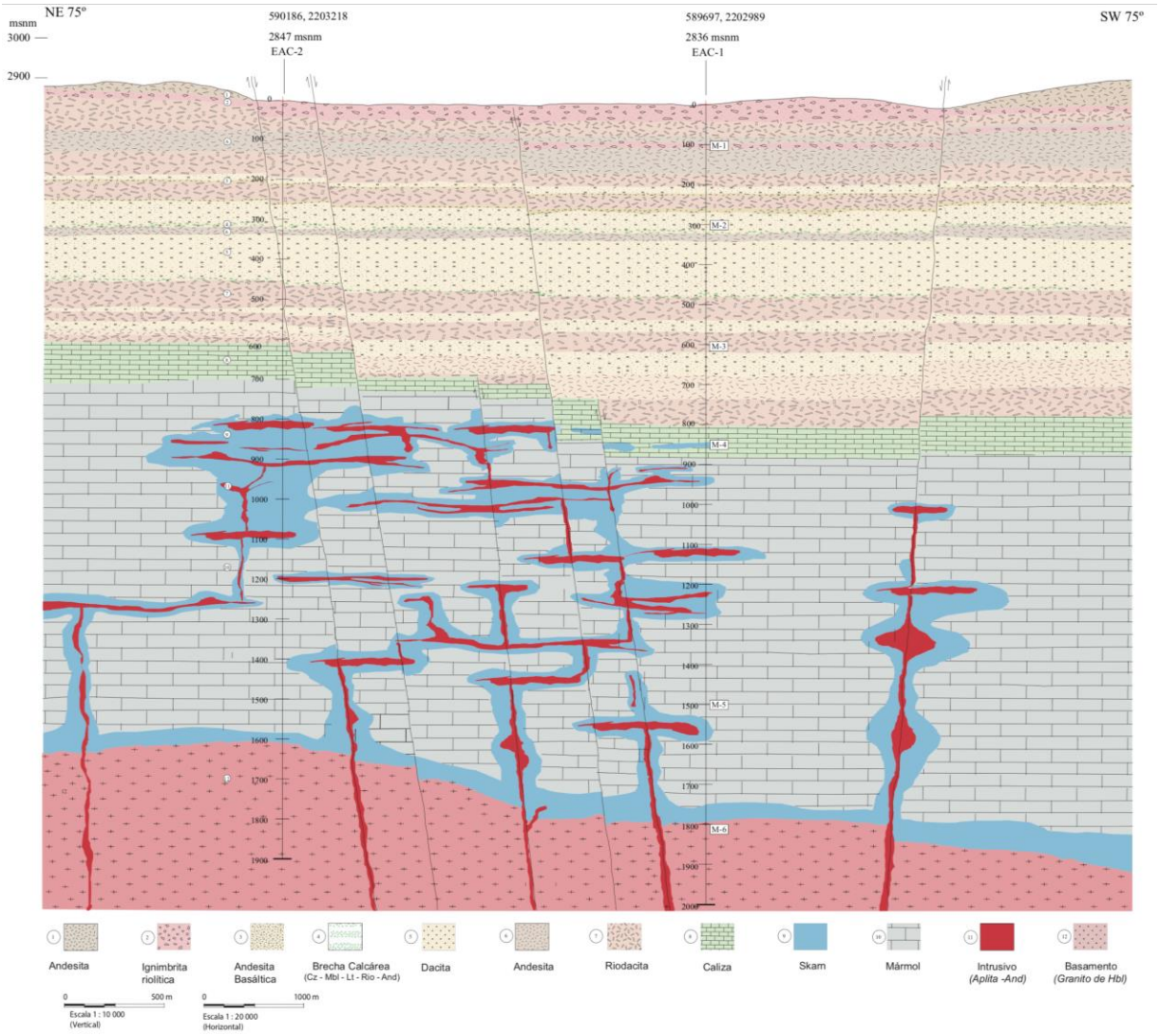

Figure 2-1. Updated stratigraphy of EAC-1 and EAC-2 by González Partida (2019) presented as a cross section.

The Acoculco area has extensively been described in other GEMex deliverables. Here only the most relevant parts for flow modelling are summarised. The general geological settings are described in D4.1 (Liotta and Garduño-Monroy (Eds.), 2019). In D3.4 (Bonté et al., 2019) an analysis of the heat source is given. The characterisation and uncertainty of the static thermal and pressure conditions was done in D6.2 (Deb et al., 2019). Also an extensive analysis was done on the local rock properties which is briefly described below (part of task 6.1 and task 7.1) and provided in D6.1 (Bär and Weydt (eds.), 2019). This includes porosity and permeability, but also thermal and mechanical characteristics of the rocks. Most analyses were done on outcrop samples, but for well EAC-1 also core material was available. An overview of the geomechanical properties was presented in D7.2 (Hofmann et al., 2020).

2.1.1 Rock properties

About 80 outcrop samples were collected inside the Acoculco caldera, in the Tenexapa and Ajajalpan canyons close to Chignahuapan and Zacatlán (Sosa-Caballo et al., 2018) and in the surrounding area of the caldera complex (Weydt et al., 2018). The volcanic rocks were related to stratigraphic units described in Avellán et al. (2018, 2020) and cover Miocene volcanic deposits of the Pre-caldera stage (Zacatlán basaltic plateu, andesitic and basaltic thrachyandesitic lavas) to Pleistocene dacitic and rhyolitic lavas (predominantly Pedernal rhyolitic lava) belonging to the Post-caldera group. The carbonatic basement is represented by Cretaceous and Jurassic limestones, shales and sandstones. For the regional 3D geological model (Calcagno et al., 2018) the volcanic rocks were merged to unit AC5. Marbles and limestones are included in unit AC4. As no outcrops of marble, skarn and granodiorite exist in Acoculco, stratigraphically equivalent outcrop samples collected in the exhumed system of Las Minas were used as analogues for the units in the deep subsurface.

More than 550 plugs were analyzed regarding petrophysical, thermophysical (see D6.1, Bär and Weydt (eds.), 2019) and rock mechanical properties (Weydt et al. submitted). Porosity (< 2%) and permeability (10^{-18} m² geometric mean) of the Cretaceous limestones is very low. The volcanic units show a higher variability. While porosity and permeability of the basaltic to trachyandesitic lavas ranges between 4 and 9% and 10^{-17} and 10^{-18} m² (geometric mean), respectively, the pyroclastic deposits show a porosity of up to 50% (Acoculco ignimbrite) and matrix permeability of up to 10^{-14} m². Furthermore, the hydrothermally altered rhyolitic lavas show the highest scattering. Here, matrix porosity ranges between ~ 10 and 60 % and matrix permeability between 10^{-16} and 10^{-13} m². In this case hydrothermal alteration increased porosity and permeability significantly.

Selected rock mechanical properties such as uniaxial compressive strength (UCS), tensile strength, static and dynamic Young's modulus and Poisson's ratio are presented in Figure 2-2. Similar to the results of the petrophysical measurements, the individual units show a wide parameter range caused by the geological heterogeneity. Fine fractures and joints filled with calcite or quartz led to a comparatively low UCS and tensile strength of the Cretaceous limestones, marbles and skarns. Likewise, hydrothermal alteration observed on the rhyolitic and Miocene andesitic outcrop samples led to reduced rock strength. With up to 400 MPa the Pleistocene Augile basaltic trachyandesitic lavas shows the highest UCS. Likewise, tensile strength of basaltic lavas belonging to the Zacatlán basaltic plateau, which overlays the carbonatic basement and of the Augile basaltic trachyandesitic lavas is almost two times higher compared to the results of the limestones, marbles and skarns. The high standard deviation of the dynamic mechanical properties can be explained due to variable sample sizes used by the different project partners.

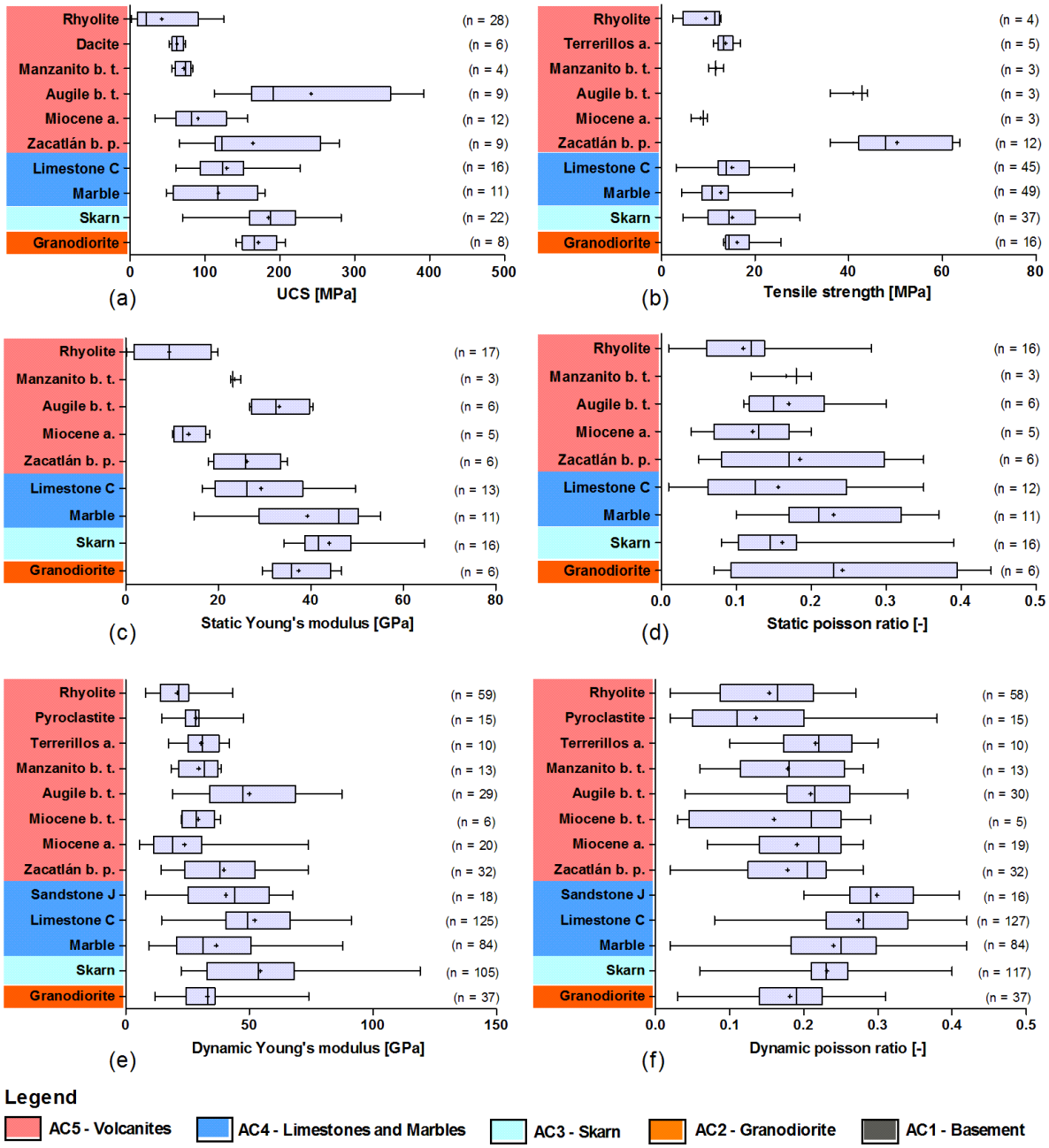

Figure 2-2. Rock mechanical properties analyzed on outcrop samples of the Acoculco geothermal field (Weydt et al., submitted). The small plus represents the mean value, while n represents the number of analyzed plugs. The colouring marks the classification regarding the regional model units as described in Calcagno et al. (2018). A = andesite, b. t. = basaltic trachyandesite, b. p. = basaltic plateau, J = Jurassic, C = Cretaceous. Data for skarn, marble and granodiorite were retrieved from outcrop samples collected in the exhumed system Las Minas.

Six drill cores have been drilled for well EAC-1, which were classified by González Partida (2019) as ignimbrite (core 1, 100 m MD), Rhyolite/Dacite (core 2, 300 m MD), Riodacite (core 3, 600 m MD), skarn (core 4, 852 m MD), marble (core 5, 1500 m MD) and granite (core 6, 1815 m MD). This classification slightly differs from Canet et al. (2015), who described core 2 as slightly altered and welded lapilli tuff and core 4 as coarse ash tuff with propylitic alteration. Earlier work (López-Hernández et al., 2009) related core 1 to the Acoculco ignimbrite, core 2 to the Cruz Colorada Dacite and core 3 to the Las Minas rhyodacite. In

contrast to the descriptions performed by González Partida (2019) and Canet et al., (2015), López-Hernández et al. (2009) classified both core 4 and core 5 as skarn.

Sample material from each core was kindly provided by CFE to perform petrophysical measurements (Table 2-1). Macroscopic description and thin section analyses performed at BGS and TU Darmstadt largely correspond to the sample classification provided by (González Partida, 2019). Core 4 was identified as intensively fractured marble. Core 3 represents tuff deposits that underwent intensive metasomatic reactions caused by Ca- and CO_2-rich fluids (40 wt % CaO, retrieved from XRF analyses), thus the sample can be classified as (endo)skarn. Matrix permeability and porosity of the reservoir core samples is comparatively low, ranging from 10^{-18} to 10^{-15} m² and ~1 to ~7 %, respectively. The cores show healed cracks and fractures (predominantly filled with calcite), especially core 4 and 5 indicate on-going tectonic activity. The permeability of the unstimulated fracture network is small, both due to filling of the fractures as result of hydrothermal circulation and to low connectivity (Lepillier et al., 2019).

Table 2-1. Selected petrophysical properties of EAC1 core samples analyzed at TU Darmstadt. The arithmetic mean is given in normal font, the numbers in bold represent geometric mean values, ± = standard deviation, () = number of analyzed plugs. ρP = Particle density, ρB = Bulk density, ϕ = Porosity, K = Permeability (Weydt et al., submitted)

Parameters	**ρP**	**ρB**	**ϕ**	**K**
Unit	[g cm^{-3}]	[g cm^{-3}]	[%]	[m²]
Ignimbrite (core 1)	2.71 ± 0,02 (2)	2.40 ± 0.003 (2)	6.53 ± 0.9 (2)	2.2E-17 ± 3.6E-18 (2)
Dacite (core 2)	2.53 ± 0,06 (3)	2.37 ± 0.02 (2)	7.43 ± 0.9 (2)	1.2E-17 ± 9.6E-18 (2)
Riodacite (core 3)	2.59 ± 0,02 (3)	2.53 ± 0.02 (2)	2.95 ± 0.9 (2)	1.1E-15 ± 7.5E-16/ **9.4E-16** (2)
Skarn (core 4)	2.69 ± 0,05 (2)	2.64 ± 0.04 (2)	1.86 ± 0.44 (2)	4.3E-17 (1)
Marble (core 5)	2.73 (1)	2.69 (1)	1.35 (1)	3.7E-17 (1)
Granite (core 6)	2.60 (1)	2.48 (1)	4.40 (1)	-

2.1.2 Structural setting

Since the best chance of creating permeability is by stimulation of the natural fracture network, information on the faults and fractures at the potential reservoir depth is essential. Near faults, the highest likelihood for a large density of fractures is present. Faults have been identified near the EAC-1 and EAC-2 wells (D4.1, Liotta and Garduño-Monroy (eds), 2019). The fault pattern of the regional Acoculco area (as well as Los Humeros/Las Minas area) are dominated by NW-SE and NE-SW oriented faults. The NW-SE striking faults are steeply dipping oblique to strike-slip faults and the NE-SW are more gently dipping oblique to normal faults. In the vicinity of the wells the NE-SW striking faults are offset by the longer NW-SE striking faults (Figure 2-3). Regionally, the opposite is also seen, indicating that the faults are formed synchronously. The interpretation from Liotta and Garduño-Monroy (eds), (2019) (D4.1) describes the NE-SW trending fault as extensional faults, whereas the NW-SE trending fault are transfer faults. The interpretation of how the faults extend in the subsurface near the boreholes is still uncertain. Different interpretations were presented at the GEMex final conference, which are illustrated in Figure 2-4. In the WSW-ENE cross sections A and B, it is shown how the NW-trending faults could intersect the wells. This interpretation is implemented in the geomodels constructed in the GEMex project (D3.1; Calcagno et al., 2020). In the alternative interpretation presented in cross section C (NW-SE cross section), it is illustrated how a SE dipping normal to normal-oblique fault (dashed line) could intersect the wells.

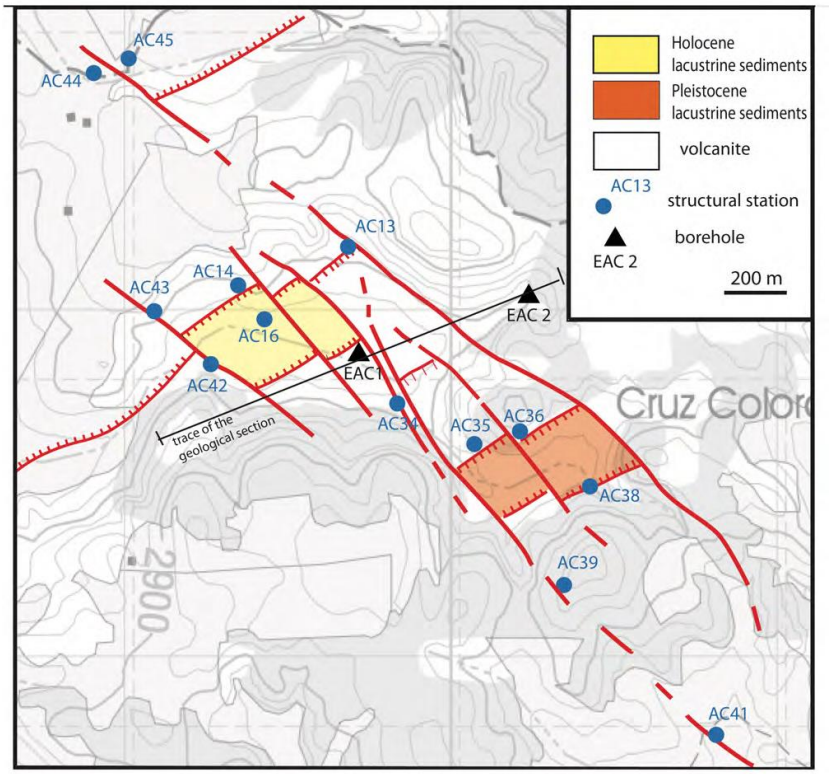

Figure 2-3. Structural map of the area where the exploration wells are located. Reproduced from D4.1 (Liotta and Garduño-Monroy (eds.), 2019).

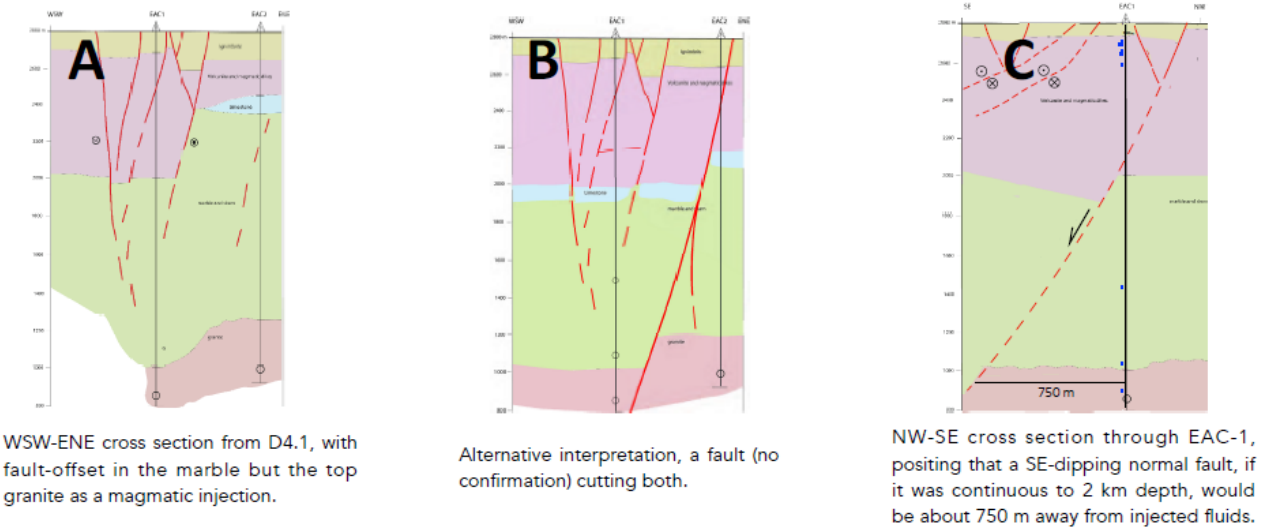

Figure 2-4. Different possible interpretations of the subsurface near EAC-1 and EAC-2. Reproduced from poster by Wheeler et al. (2020).

Information on the potential fracture architecture and density has been derived mainly from outcrops (D4.1, Liotta and Garduño-Monroy (eds), 2019; Lepillier et al., 2019; Bastesen et al., 2020). Due to differences in burial, local deformation, temperature and hydrothermal alteration, differences are to be expected between the fractures in outcrops and in the potential reservoir. A summary of the fracture characteristics for relevant formations was presented at the GEMex final conference as a poster presentation (Bastesen et al., 2020). In

Figure 2-5 some results from the poster are reproduced, which show inferred fracture transmissivity estimates for limestones, marble and granite/granodiorite. Fracture intensities in the marble and the plutonic rocks are expected to be very low compared to surface rocks. For the marble (and granodiorite), a dominantly low permeability was observed in the field with mostly fractures related to uplift/unloading, however in fault zones and surrounding dykes the fracture intensity is significantly higher. In the same study fractures in lava flows, volcanic tuffs and sediments (limestones) shows a significantly higher fracture frequency indicating a more complex burial and unroofing history.

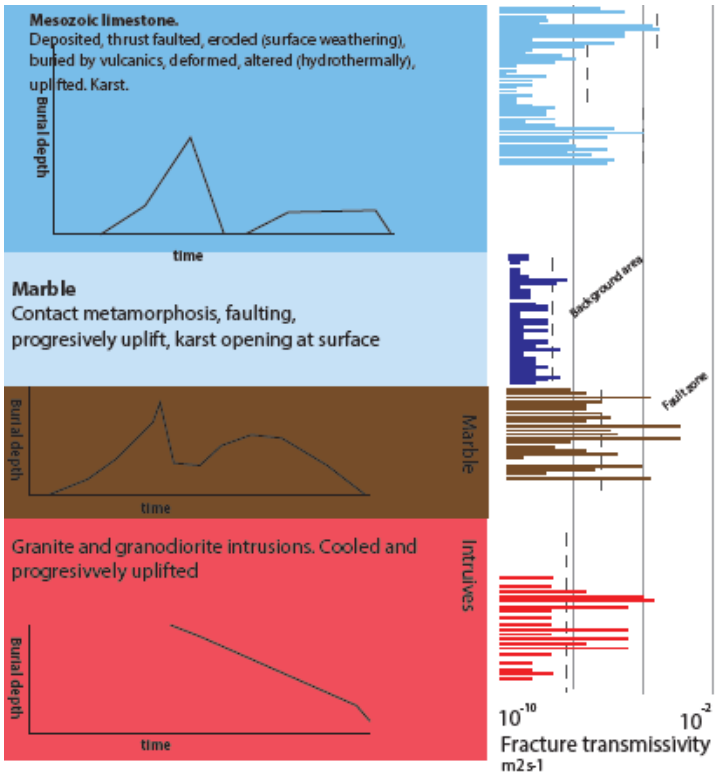

Figure 2-5. Pseudo well of the main units in the two calderas. Fracture frequencies in the outcrop analogues. Permeability is based on hydrogeological values for different fractured medias. Flow has not been tested in field. From (Bastesen et al., 2020).

A quantitative analysis was done for outcrops of limestone, marble and skarn using scanline surveys (Lepillier et al., 2019), in which all fractures were counted along scanlines and the fracture height and aperture observed. The fracture count for limestones was the largest, followed by skarn and marble (Lepillier et al., 2019). In total 7 fracture sets were identified with different dip and orientations. Based on the fracture sets, 2D discrete fracture networks (DFN) were created. Fluid and heat flow in these fractures networks was simulated using Finite Element Method software. From the simulation, it was clear that the fracture networks were poorly connected, which results in a low permeability. For some outcrops of marble, fractures were relatively long and connectivity was better (Lepillier et al., 2019). For 3D conditions connectivity is likely to be better.

In (Kruszewski et al., 2020 in review), the in-situ stress conditions were analysed. The study was based on currently available information, which includes the borehole logs and drilling reports of the two exploration wells EAC-1 and EAC-2, including Formation Integrity Tests (FIT) and fluid loss information. From the World Stress Map (Heidbach et al., 2016) the direction of the maximum in situ stress S_{H_max} is N55. Based on the computed relations between S_{hmin} and S_v it is speculated that the stress conditions of the EAC-2 well are between normal ($S_V > S_{Hmax} > S_{hmin}$) and strike-slip ($S_{Hmax} > S_V > S_{hmin}$) faulting regime (Figure 2-6).

From the geological analysis, the paleo stress regime was interpreted as a normal to strike-slip stress regime, following a period dominated by oblique right lateral movement.

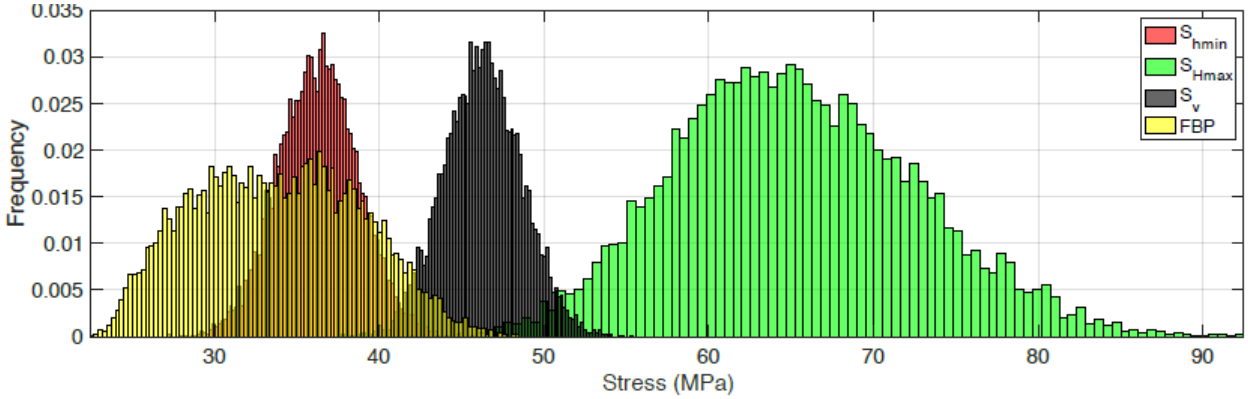

Figure 2-6. Superimposed frequency histogram of mean in-situ principal stresses and stimulation pressures at a depth of 1830 m MD (Kruszewski et al., 2020 in review) (FBP = Formation Breakdown Pressure).

A further important characteristic for determining the potential of the site for EGS is the temperature. Temperature was measured in the two exploration wells EAC-1 and EAC-2 (D6.2, Deb et al, 2019 and D3.4, Bonté et al., 2019) including a log after 312 hrs after circulation of the drilling mud was stopped. The measured temperatures in the two wells are consistent and indicate a temperature of around 300 °C at a depth of 2000 m with a slightly lower temperature at EAC-2 than EAC-1. Regional estimates of the basal heat flow are highly variable and range from 35 to more than 100 mW/m^2, with a best estimate of 91 mW/m^2 (Deb et al., 2019). The basal heat flow near the granite intrusion was estimated in the range of 360 mW/m^2 to 400 mW/m^2 using numerical simulations (Deb et al., 2019).

2.2 Previous EGS production estimates in Acoculco

Based on preliminary results from the GEMex project, first estimates of the potential production resulting from EGS stimulation have been reported in D6.2. A hydraulic fracture was assumed to be created between EAC-1 and EAC-2 with a stimulated zone of 100 m wide around the fracture. It was assumed that the potential fault(s) in between the EAC-1 and EAC-2 wells did not pose a barrier to the hydraulic fracture or the flow. Two fracture heights were investigated (100 m and 300 m) at two different depths: at 950 m depth in the skarn and at 1700 m depth in the granite/granodiorite. All the simulations were tested with three circulation rates: 10 l/s, 30 l/s and 50 l/s (constant over time). Figure 2-7 shows the thermal field after 30 years of production from the skarn reservoir for one of the investigated scenarios.

Permeability values for the fracture zone were based on literature and were decreased from the centre of the stimulation to the edge. For example, in Soultz-Sous-Forêts (Vogt et al., 2012), the permeability range estimated is in the order of 10^{-12} m² to 10^{-14} m² (corresponding approximately to 1 D – 10 mD) decreasing from the stimulation centre to the edges. Other studies show even lower permeability realized from stimulation (Gholizadeh Doonechaly et al., 2013).

The producible geothermal volumes (stimulated volume connecting the two well) were in the order of 0.036 km^3 and 0.012 km^3, which are smaller than the values of 0.1-0.3 km^3 reported by Jung (2013) as being required for commercial development. The results showed that only for the fracture height of 300 m very fast breakthrough of cold water could be avoided. Also quite high permeability needs to be used if wells are connected only via a single vertical fracture as shown in previous studies (e.g. Hofmann et al. 2014). For lower permeability, transmissivity of the fracture zone is too small to allow commercial rates.

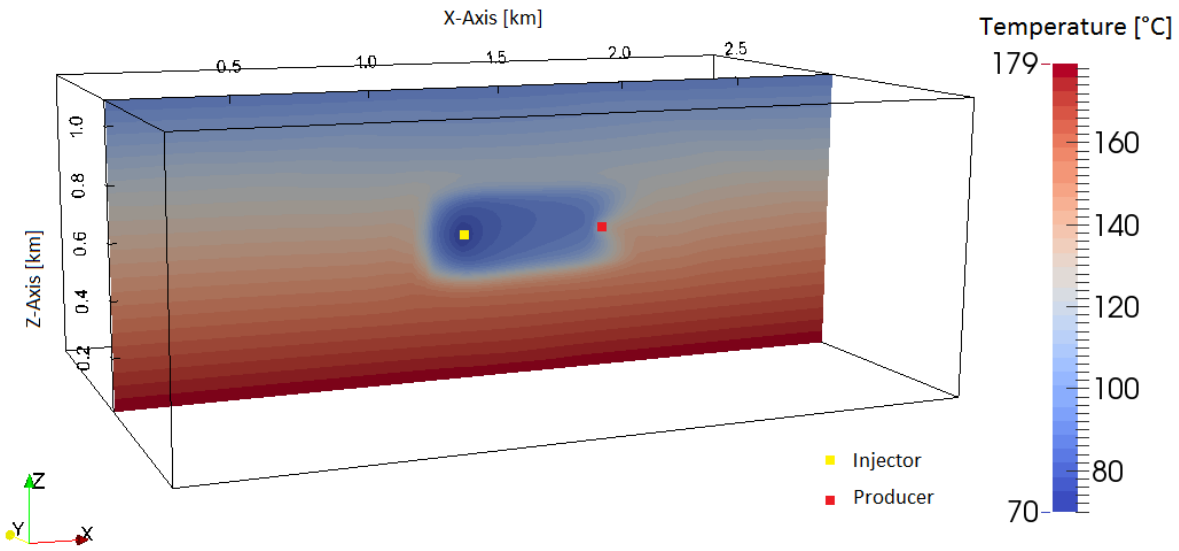

Figure 2-7. Temperature distribution within the larger skarn reservoir after 30 years of production in the low permeability scenario of 10^{-13} m² for a circulation rate of 30 l/s, the injector and producer stimulation points are indicated by yellow and red respectively. Reproduced from D6.2.

3 Simulation approach and model description

3.1 Description of the scenarios

Based on the work reported in D7.2 (Hofmann et al., 2020) and on discussions with the Comisión Federal de Electricidad (CFE) and the Mexican GEMex consortium, EAC-1 was selected as the first target for stimulation. This well is most likely to be close to faults and fractures in the subsurface. Stimulation concepts have been developed in D7.2, but for most concepts details of the achieved stimulated area and permeability were not specified, largely because of the considerable uncertainty. However, for the production estimates, the (anisotropic) permeability and the spatial distribution of the permeability are the main required input. Therefore instead of attempting to implement the concepts from D7.2 directly, stimulation concepts were identified based on the potential permeability created. Depending on the subsurface characteristics, permeability could be created (or enhanced) in four different ways:

1. Hydraulic fracture: In case there are very few natural fractures, fractures are poorly connected or the fracture sealing is not easy to stimulate, a single, vertical hydraulic fracture could be the result of a stimulation. In this case, a single tensile (Mode I) fracture is assumed. There are two possibilities:
    a. The growth of the hydraulic fracture is assumed to be constrained in the vertical direction. Input for this scenario is mainly taken from the MFrac stimulation scenarios for EAC-2 from D7.2, chapter 4. Permeability is assumed to be created from the use of acid, from some slip movement on the fault or from the use of proppants.
    b. There is no limit on the growth of the hydraulic fracture in vertical direction (unconstrained). The input is taken from D7.2, chapter 3. From the estimated fracture half length (<100 m) and the previous estimates of the production, it is clear up front that the temperature will not be sustainable in such a case. The scenario is added for completeness.

2. Stimulated fracture network: the second option is that a fracture network is stimulated. Resulting permeability will depend on the level of connectivity and density of the fracture network as well as the reactivation level. Shape of the stimulated area and orientation of the permeability also depends on the in-situ stress field.
3. Reactivated fault zone: If a fault crosses a well, it is also possible that a fault zone is stimulated. This will most likely result in a relatively narrow zone of high permeability along the fault. Cross-fault permeability is likely to be much lower than along-fault permeability.
4. Finally a combination might result in which both fractures and a fault are stimulated.

For stimulation concept 3, the permeability depends crucially on which fault is intersected. From the direction of the minimum in-situ stress estimated from EAC-2 (Kruszewski et al. 2020 (in review)), the normal, SW-NE trending faults are most likely to be re-activated. However, as discussed in the site description, these faults are separated in smaller faults due to the large strike-slip/oblique-slip NW-SE trending faults and surface mapping showed the NW-SE trending faults to be most conductive (Bastesen et al., 2020). Moreover in the geological model from GEMex Task 3, no normal faults cross the wells at depth. Therefore it has been assumed for stimulation concept 3 that the reactivated faults are the large, continuous NW-SE trending faults, which in the geological model intersect the EAC-1 well at different depths. For the estimation of the potential for induced seismicity (Chapter 5), some scenarios were run in which the normal, SW-NE striking faults are reactivated.

These four stimulation concepts can be combined with different depths to arrive at development scenarios. Three different depths are selected in line with the stimulation concepts from D7.2:

- Open hole stimulation: in effect the stimulation will most likely be just below the casing at the limestones at 800 m AH depth. Around this depth (850-853 m), fractures filled with calcite and pyrite where identified by Gama et al. (1995) in well EAC-1.
- Stimulation at approximately 1500 m AH depth in the skarn/marbles. In D7.2 two depths were identified, but to reduce the simulation load, only one depth is selected here.
- Stimulation at the top of the granite/bottom skarn at around 1800 m depth.

To complete the development scenarios, a number of assumptions are required:

- There is no significant permeability outside of the stimulated areas (D6.1, Bär and Weydt (eds.), 2019)
- Main direction of permeability is perpendicular to the direction of least principal stress (S_{hmin}).
- No natural recharge occurs.
- Since there is no natural recharge, in order to have an operational system a second well is introduced. This second well is placed near the stimulated zone of the first well and also stimulated so that the stimulated zones overlap. The second well is placed in the direction in which the main permeability develops and has exactly the same stimulation as the first well. Such a scenario could be achieved if during stimulation of the first well, micro-seismic monitoring is used to identify where permeability is created (assuming a direct correlation between observed seismicity and permeability)(e.g. Audigane et al., 2002)

In Table 3-1 an overview of the development scenarios is presented, including the stimulation depth, the stimulation concepts and position of the second well. For the depth of 800 m, it became clear that only stimulation concept 2 resulted in a useable development scenario. This will be discussed in section 4.1.

Table 3-1. Overview of the development scenarios

Sc number	Stimulation depth	stimulation concept	Position of 2nd well
1.1a and b	800 mMD	Hydraulic frac	NE dir
1.2	800 mMD	Stimulated frac network	NE dir
1.3	800 mMD	Reactivated fault	Along the fault in NW dir
1.4	800 mMD	Combined reactivated fault and fracture network	NE dir
2.1 a and b	1500 mMD	Hydraulic frac	NE dir
2.2	1500 mMD	Stimulated frac network	NE dir
2.3	1500 mMD	Reactivated fault	Along the fault in NW dir
2.4	1500 mMD	Combined reactivated fault and fracture network	NE dir
3.1 a and b	1800 mMD	Hydraulic frac	NE dir
3.2	1800 mMD	Stimulated frac network	NE dir
3.3	1800 mMD	Reactivated fault	Along the fault in NW dir
3.4	1800 mMD	Combined reactivated fault and fracture network	NE dir.

3.2 Simulation approach

3.2.1 Flow and heat modelling

The approach to simulate the development scenarios is not very detailed in representing all the processes in the subsurface and wells. Instead a relatively fast reservoir simulation tool was selected because, at this stage of development the uncertainty is still so high, that many possible scenarios/uncertainties need to be evaluated. The main uncertainty for the estimation of the potential production, is the uncertainty in the size and permeability of the stimulated area. This uncertainty has been included in the analysis via a combination of scenarios (section 3.1) and stochastic modelling (discussed in section 3.3). However, for the estimation of the production other properties also play a role, for which the uncertainty is not taken into account, such as:

- Rock properties prior to stimulation (matrix permeability and porosity)
- Thermal rock properties (heat capacity, thermal conductivity)
- Temperature and pressure prior to production
- Fluid composition and properties (both injection and in situ)
- Groundwater flow / recharge
- Basal heat flow and radiogenic heat production

In addition to the uncertainty in the downhole characteristics, the process of modelling impacts the accuracy of the results: gridding, solution accuracy, but more importantly which processes are accounted for or not. Since the uncertainty is quite high, the aim is to simulate many scenarios, therefore the model approach is simplified. The following aspects are not included in the reservoir simulations:

- Changes in permeability due to temperature or pressure are not included. The impact of pressure via changes in effective stress was estimated to be small except for the limestone (Lepillier et al., 2019). Impact of temperature is localized around the injector.
- Changes of the permeability over time for example due to chemical processes or due to degradation of proppants are not accounted for.
- Flow inside the fractures is not simulated explicitly, but only an effective, bulk permeability is used (Darcy flow only)
- One amalgamated permeability for both matrix and fractures, instead of dual porosity/dual permeability
- Basal heat flow and radiogenic heat production are not accounted for.
- The fluid properties density, thermal conductivity and specific heat capacity are not dependent on temperature.

The simulator used for the flow and heat simulation in the reservoir is ECLIPSE ® 100 (Schlumberger, 2018) with Temperature option, because it is a fast simulator and is well suited for incorporation of geologically realistic geometry, including faults.

3.2.2 Geomechanical modelling

Based on the simulated pressure and temperature changes over time from the reservoir simulator, the induced stresses along pre-existing faults are modelled using an in-house TNO-developed semi-numerical approach coined as MACRIS (Mechanical Analysis of Complex Reservoirs for Induced Seismicity, see (van Wees et al., 2019)). The induced seismicity is estimated based on the modelled stresses using Dieterich's approach (1994). The main specificity of MACRIS is that it is a mesh-free approach where there is no need to build a dedicated grid for the geomechanical analysis. MACRIS takes the grids of the reservoir flow simulation directly as input.

MACRIS honors:

- The complex geometry of the reservoir and pre-existing faults;
- The direct changes in effective normal stress at faults due to changes in fault pressure,
- The induced poroelastic stress changes due to the reservoir deformation when the reservoir pressure is changed; typical values of the Young's modulus and Poisson's ratio are kept constant for all the simulations presented in this section, and both elastic properties are kept vertically homogeneous;
- The induced thermoelastic stress changes due to the reservoir deformation when the reservoir temperature is changed; the thermal expansion coefficient is kept constant and equal to 3×10^{-5} K^{-1} for all the simulations presented in this section.

The traditional Coulomb failure model predicts that whenever the Coulomb stress reaches the failure line, the fault can be reactivated, and an earthquake might be generated. Changes in Coulomb stress ΔS are given as:

$$\Delta S = \Delta\tau - \mu_f \Delta\sigma_n' \qquad (1)$$

where $\Delta\tau$ and $\Delta\sigma_n'$ are respectively the changes in shear stress and effective normal stress, and μ_f is the coefficient of fault friction. This Coulomb failure model leads to a direct proportionality between the seismicity rate and the Coulomb stress rate. It means that during any arbitrary stressing history, as soon as

the Coulomb stress starts to decrease, the Coulomb failure model predicts an instantaneous shut-down of the seismicity. This prediction is not in agreement with the observed seismicity, which generally shows a gradual decay following the onset of Coulomb stress decrease.

In the following we relate the seismicity rate with the Coulomb stressing rate following the seminal work of Dieterich (1994) where:

$$R_d = \frac{r_0}{\gamma \dot{S}_0} \quad \text{with} \quad \frac{d\gamma}{dt} = \frac{1}{A\sigma_n'}\left[1 - \gamma \frac{dS}{dt}\right] \tag{2}$$

where R_d is the seismicity rate, γ is a state variable, S is the Coulomb stress as defined in equation 1. The constant r_0 is the steady-state background seismicity rate at the reference stressing rate $\dot{S}_0$. A is a dimensionless fault constitutive parameter. Segall and Lu (2015) reformulated this seismicity rate equation to eliminate the state variable γ. They defined a normalized seismicity rate, relative to the background rate, as:

$$R = \frac{R_d}{r_0} \tag{3}$$

The differential equation for R, derived from equations (2) and (3), is:

$$\frac{dR}{dt} = \frac{R}{T_a}\left[\frac{\dot{S}}{\dot{S}_0} - R\right] \tag{4}$$

where $T_a = A\sigma_n'/\dot{S}_0$ is the characteristic time delay for the earthquake nucleation process. It implies that the Dieterich (1994) theory honors the frictional constitutive behavior of faults, which is a crucial ingredient that is missing in the initial Coulomb failure model. More specifically, the Dieterich (1994) theory reproduces the fact that the onset of frictional sliding is a non-instantaneous time-dependent process (as opposed to the instantaneity assumption of the Coulomb model), which introduces a time-dependent failure mechanism for the generation of earthquakes. It also means that faults in Dieterich's seismicity rate theory are thus always active, generating events, although at a very low rate if the background stressing rate $\dot{S}_0$ is very low, as in Groningen for example (see Candela et al. 2019). In contrast, in the Coulomb failure model, faults are only reactivated after reaching a certain threshold.

The normalized seismicity rate R in equations 3 and 4 represents the seismicity rate relative to the background seismicity rate r_0. As an example, an R of 1000 indicates an increase of one thousand-fold of the seismicity rate relative to the background seismicity rate.

3.3 Implementation of the development scenarios

For each of the identified development scenarios, 50 realizations were run instead of a single realization. The parameters that were varied to create the realizations were the size and permeability of the stimulated area. These were sampled from (normal) distributions. The permeability was also sampled from a normal distribution instead of a lognormal distribution, because in this case the fracture density is a main factor determining the permeability, which is normally distributed.

The values for the permeability *k* in the three main grid directions *i*, *j* and *k* were sampled separately. The average of the distributions from which the values were sampled, have fixed ratios between the different directions: maximum horizontal, minimum horizontal and vertical direction. The direction of the maximum

horizontal permeability depends on the stimulation concept. For stimulation concepts 1 and 2 (hydraulic fracture and stimulated fracture network) the maximum horizontal permeability is in NE direction (direction S_{Hmax}). For stimulation concept 3, the direction of the maximum horizontal permeability is along the reactivated fault. For stimulation concept 4, it is a combination of concepts 2 and 3. The average vertical permeability was always 50% of the average maximum horizontal permeability; the average minimum horizontal permeability was always 10% of the average maximum horizontal permeability. The average permeability ($\bar{k}$) and standard deviation (s_k) of the distributions are thus:

$$\bar{k}_{max} = \bar{k} \text{ and } s_{k,max} = s_k$$

$$\bar{k}_{min} = 0.1\bar{k} \text{ and } s_{k,min} = 0.1s_k$$

$$\bar{k}_{vert} = 0.5\bar{k} \text{ and } s_{kvert} = 0.5s_k$$

The values of $\bar{k}$ and s_k per scenario are listed in Table 3-2.

A main challenge was the choice for the values for the different scenarios. Currently there is hardly any control on the potential permeability or the size of stimulated area. Only for the hydraulic fracturing scenarios, there is input on the hydraulic fracture growth in terms of length and height from D7.2. The main factor determining the fracture dimensions is the fracture height growth. This was captured with two different scenarios: 1a and 1b. Since the difference for different depths was limited, the same distributions for fracture length and height were used for all depths. The fracture dimensions selected here are in general smaller than those in D7.2, because upon closure of the fracture generally the size decreases, which was not simulated in D7.2. Also, from the acid stimulation simulations some estimates for the fracture conductivity can be derived. The range of conductivity was 1000 mDm to 100.000 mDm (maximum value at the well before closure). Therefore an average conductivity of 10.000 mDm was used (400 mD x 25 m grid width).

For the other scenarios, well founded values are not possible, because so many factors are still unknown. For skarn and marble some information is available of fracture density from outcrops (D4.1; Lepillier et al., 2019). However, fracture aperture is highly uncertain. Also, for the limestone and marble, impact of possible chemical stimulation is difficult to predict at this point in time, since only acid in combination with hydraulic fracturing was tested (see also D7.2).

Therefore values were selected based on expert judgement and realised permeability in other EGS stimulations (e.g. Audigane et al., 2002; Vogt et al., 2012). The values reflect what might be achieved given a successful stimulation programme. The results should therefore in no way be interpreted in absolute terms, but only to indicate trends and possible outcomes.

Minimum and maximum bounds were enforced on the parameters. These were essentially for numerical purposes, because very extreme values in many scenarios caused numerical problems.

Table 3-2. Overview of the average and standard deviation of the probability distributions for size and bulk permeability of the stimulated area for all scenarios.

Scenario	Variable	Average	Standard deviation	Minimum/Maximum
1.1a / 2.1a / 3.1a	Half length	200 m	50 m	100 / 400 m
	Half height	100 m	25 m	50 / 200 m
	Permeability $\bar{k}$	400 mD	100 mD	100 / 4000 mD
2.1b / 3.1b	Half length	75 m	20 m	40 / 150 m
	Half height	300 m	50 m	200 / 400 m
	Permeability $\bar{k}$	400 mD	100 mD	100 / 4000 mD
1.2 / 2.2 / 3.2	Half length	200 m	50 m	50 / 300 m
	Permeability $\bar{k}$	200 mD	50 mD	10 / 2000 mD
3.3	Half length	500 m	125 m	100 / 1000 m
	Permeability $\bar{k}$	400 mD	100 mD	100 / 4000 mD
2.4 / 3.4	Half length stim. Frac. network	200 m	50 m	100 / 300 m
	Half height/length stimulated fault	500 m	50 m	400 / 600 m
	Permeability $\bar{k}$	200 mD	50 mD	10 / 2000 mD

Further details of the implementation in the numerical simulator are given below:

- Impact of discontinuities such as layering is not accounted for.
- The permeability in the stimulated areas decreases linearly with distance from well. Thus the sampled values are the maximum permeability values at the well.
- For stimulation scenarios 1 and 3 the width of the stimulated area is always 1 grid block (~25 m). The fault damage zone observed in outcrops was less than 20 m (Kruszewski et al., 2020 in review), but these were faults with limited offset. For larger off set faults in the subsurface in the caldera, larger damage zones are well possible (Hofmann et al., 2020, D7.2).
- For stimulation scenario 3.3, to ensure that a fault crosses the well at the right depth, the fault dip has been increased by 5 degrees from the base case.
- For stimulation concepts 2, 3 and 4, the stimulations are implemented as if originating from a single point along the well (nucleation point). The depth of the nucleation point is taken shallower than the stimulated depth because the simulations in D7.2 shows that fractures tend to grow upwards. This has been done for all scenarios. The point is shifted up by 50% of the half height. See Figure 3-5 for an illustration of the resulting stimulated area.
- For stimulation concept 1, the stimulation is assumed to occur over the entire height of the stimulated area. This is not more realistic than a single realization point, but has been done for numerical reasons.

- The stimulated areas of the two wells are assumed to overlap. The amount of overlap depends on the size of the stimulated area.
- the completion in the second well is always taken the same as in EAC-1 (open hole below 800 m).

3.4 Model description

3.4.1 Geological input

The geological input was based on the local structural model as prepared in GEMex WP3 (Calcagno et al., 2020). The final version of the model (Figure 3-1), which integrates all the outcomes from field work and geophysical surveys, became available in April 2020 and is described in Deliverable 3.1 (Calcagno et al., 2020). See D5.10 and D5.12 for discussion on the integration of the geophysical data. Please note that for this model, the stratigraphy as presented in (Lorenzo Pulido et al., 2010) was used.

For this work, a preliminary version of the model was used which became available in June 2019 (Described as 'second geomodel update' in D3.1). The main change in the final model compared to the model from June 2019 is that the surfaces near the wells have changed: they are matched better now to the stratigraphy at the well locations. The preliminary model from June 2019 did not match well the stratigraphy at the well locations. Also a fault to the north of the wells was added (Alcaparrosa fault). When the final model became available in April 2020 it was decided not to redo all the simulations, because:

- It was too late for incorporation in this work since the project ends 31 May 2020.
- The faults near the wells are the same. The Alcaparrosa fault is too far away from the wells to be included in the simulation model.
- The surface of the limestone intersects the surface of the skarns (or shows a hole) at the locations of the wells. This is very problematic for a simulation grid. To make a simulation grid would require manual editing which would destroy the fit to the well logs.

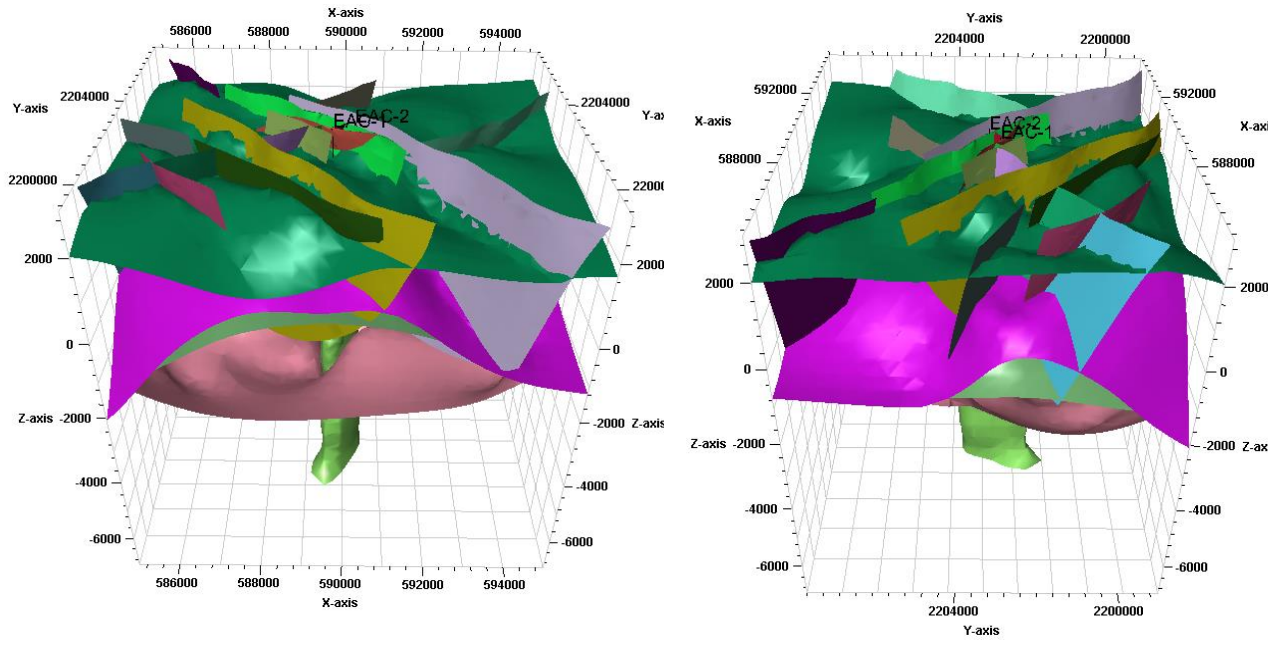

A. View from South B. View from West

Figure 3-1. Illustration of the final local geological model from WP3.

For the Acoculco local structural model, a fault model and five surfaces were provided. The surfaces are: bottom of the volcanites, limestone, skarn/marbles, granite and the basement of the model (Figure 3-2). The surface area of this model covers approximately 10 x 8.5 km. The depth range is more than 3 km.

For the simulation of the development scenarios, a simulation model was created based on the surfaces and faults provided. The following choices were made:

- The area was decreased to 2.5 x 2.5 km (Figure 3-2)
- The depth range of the model is from the bottom of the volcanites down to sea level. Thus the volcanites are not included in the model.
- Only two major NW trending, oblique faults near well EAC-1 are incorporated. For scenario 3.3 the dip of the faults is increased by 5° compared to the dip in the geological model provided. This was done to ensure that a fault crosses the well at the right depth.
- The grid is aligned to the NW trending faults and grid block size is 25 x 25 m
- In the vertical direction, grid block thickness ranges from 15 to 65 m (41 m on average).

These choices result in a grid with 610,000 active grid blocks (100 x 100 x 61) (Figure 3-3 and Figure 3-4).

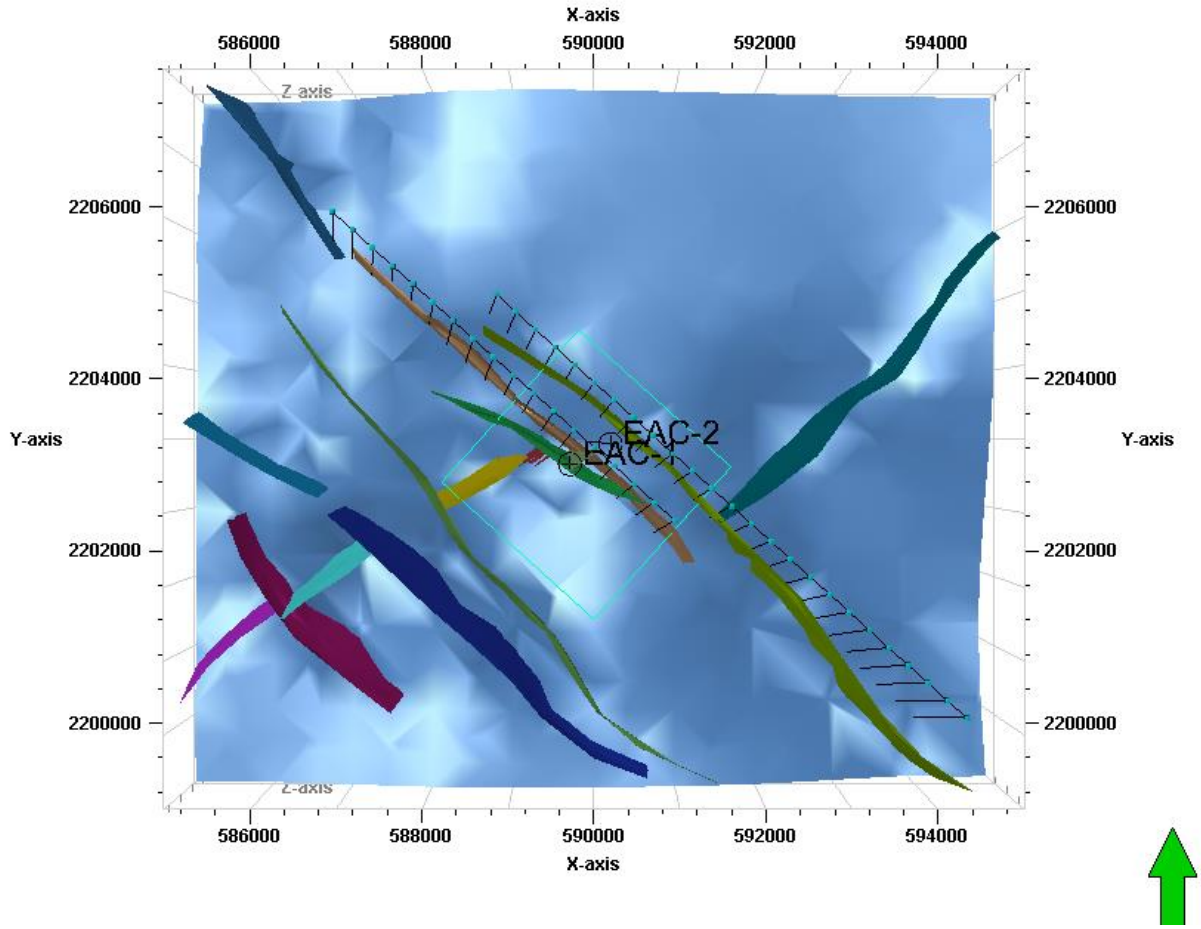

Figure 3-2. Top view of the input surfaces and faults. The rectangle indicates the model area of the simulation model created in this work. Also shown in black is the representation using fault pillars of the two NW-trending faults included in the model.

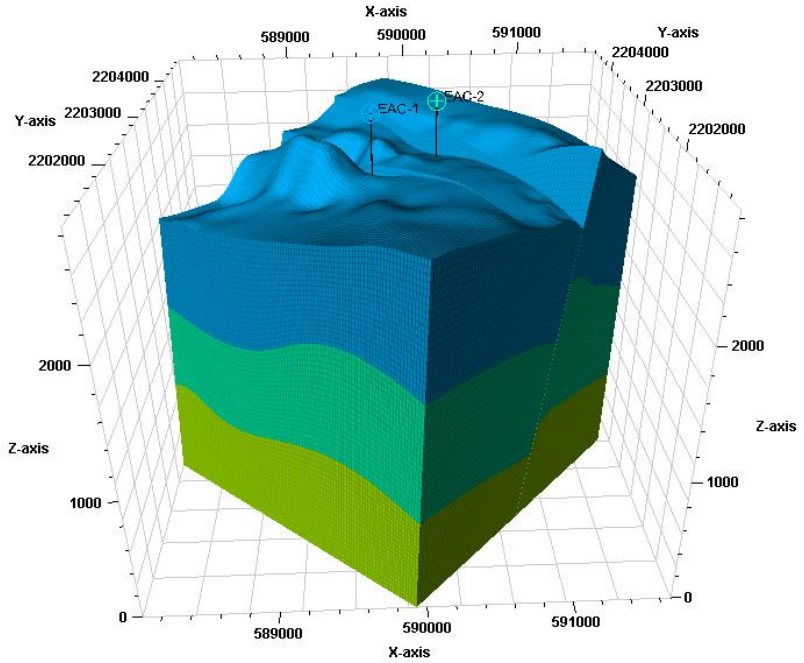

Figure 3-3. Simulation grid showing three zones (from top to bottom: limestone, skarn/marbles, granite).

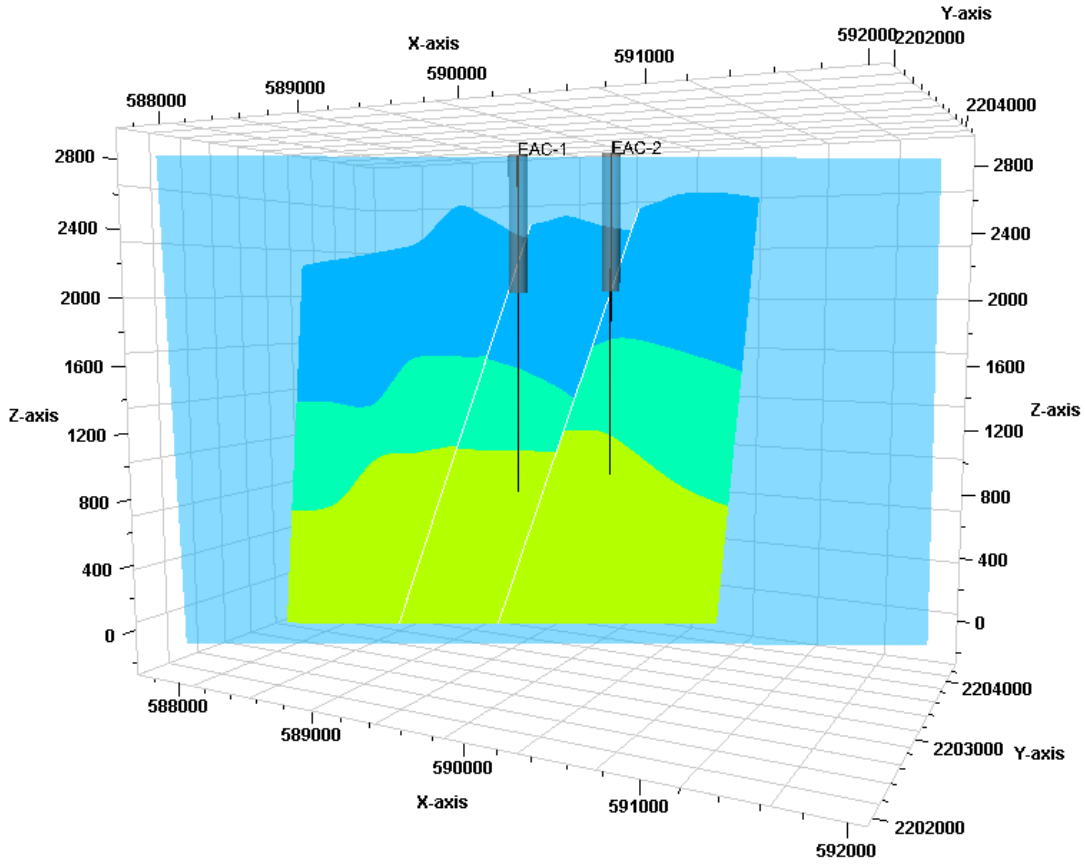

Figure 3-4. Cross section through wells EAC-1 and EAC-2 of the simulation grid (from top to bottom: limestone, skarn/marbles, granite).

Stimulated permeability

The input for the stimulated permeability has been described in Section 3.3. An illustration of the stimulated permeability is given in Figure 3-5. The figure shows the area for each scenario in which the permeability is increased compared to the background permeability.

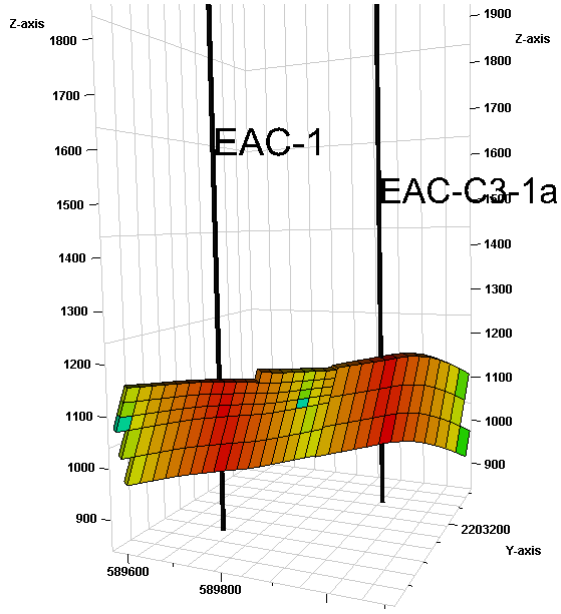

A. scenario 3.1a

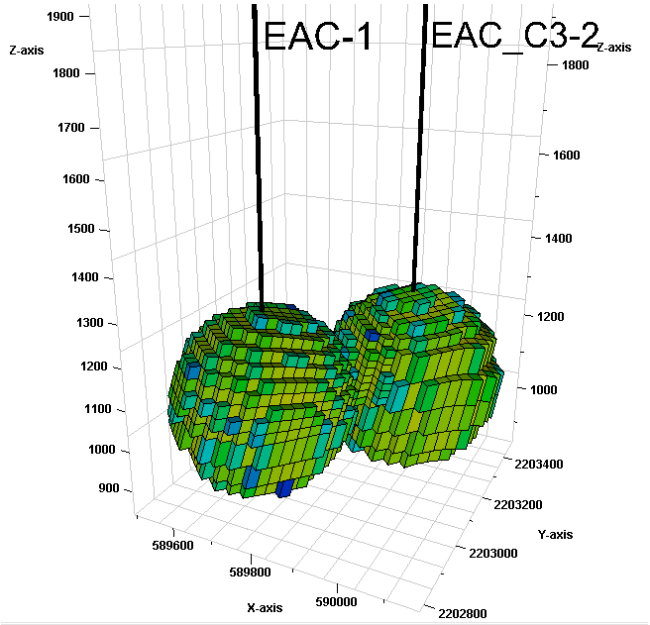

B. scenario 3.2

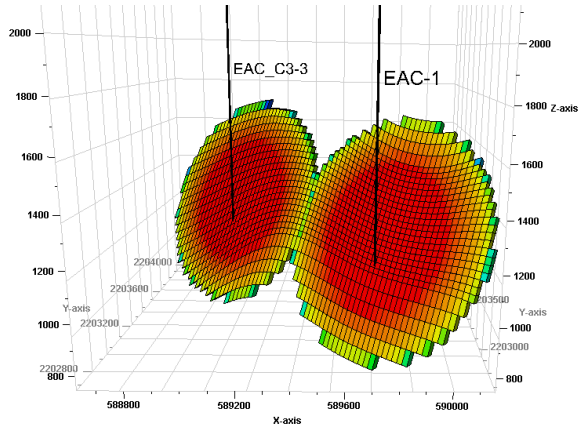

C. scenario 3.3

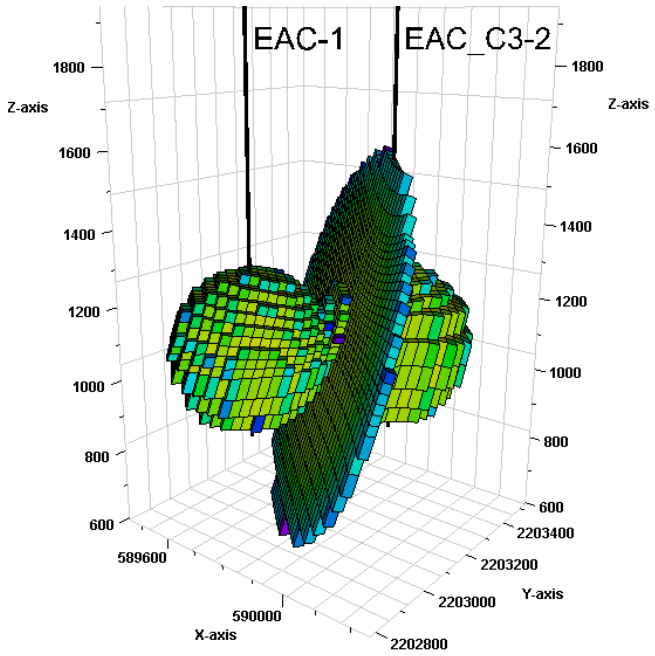

D scenario 3.4

Figure 3-5. Illustration of the stimulated permeability for the four stimulation concepts at stimulation depth 3 (1800 mMD) 1. A: scenario 3.1a, B: scenario 3.2, C: scenario 3.3, D: scenario 3.4. Cooler colors are lower permeability

Models for induced seismicity simulation

In a later stage of the work, two slightly adjusted models were created for induced seismicity simulation and sensitivity analysis simulation: one with the same NW trending oblique to strike-slip faults as the main model (referred to as strike-slip fault model) and one with NE trending normal faults (referred to as normal-slip fault model). The two models are simplified in one main characteristic: instead of the actual surfaces describing the boundaries between the formations, a box model was created with horizontal layers (compare Figure 3-6A and Figure 3-6B). The advantage of the box model is a more regular grid, which allows for more detailed simulation of the fault (Section 4.2) and better coupling to the geomechanical model (Chapter 5). The division between the layers was based on the interpretation of well EAC-1 used in WP 3 (D3.1). A new interpretation of the formations in the wells has been made later by Eduardo González-Partida (González Partida, 2019). In Table 3-3 the interpretation from González-Partida (2019) is compared to the values used in the box model. This comparison shows that the main difference is in the interpretation of the limestone. This is partially caused by the choice not to include the volcanites in the model. The limestone was assumed to extend to the top of the model.

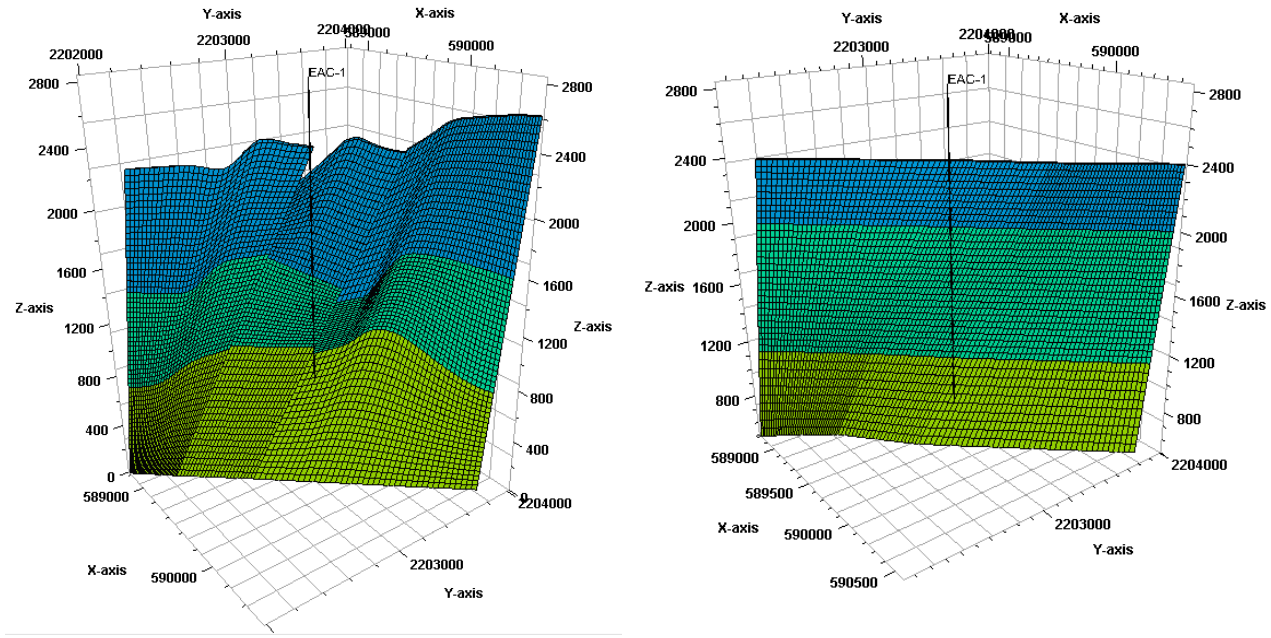

A B

Figure 3-6. cross section of the dynamic simulation model used for the development scenarios (A) and for the sensitivity analysis of the fault and induced seismicity calculations (B) showing from top to bottom: limestone, skarn/marbles, granite.

Table 3-3. Comparison of the top of the different layers in the box model and as identified in (González-Partida, 2019).

	Box model	**(González-Partida, 2019)**	
		EAC-1	EAC-2
Top limestone	400 m AH (Top model)	800 m AH	610 m AH
Top skarn/marble	800 m AH	900 m AH	700 m AH
Top granite	1650 m AH	1800 m AH	1600 m AH

For the stimulated permeability of the model with strike-slip faults, the same approach as in scenario 3.3 was used: the fault intersecting the well at approximately 1800 m depth was stimulated. The resulting permeability is shown in Figure 3-7.

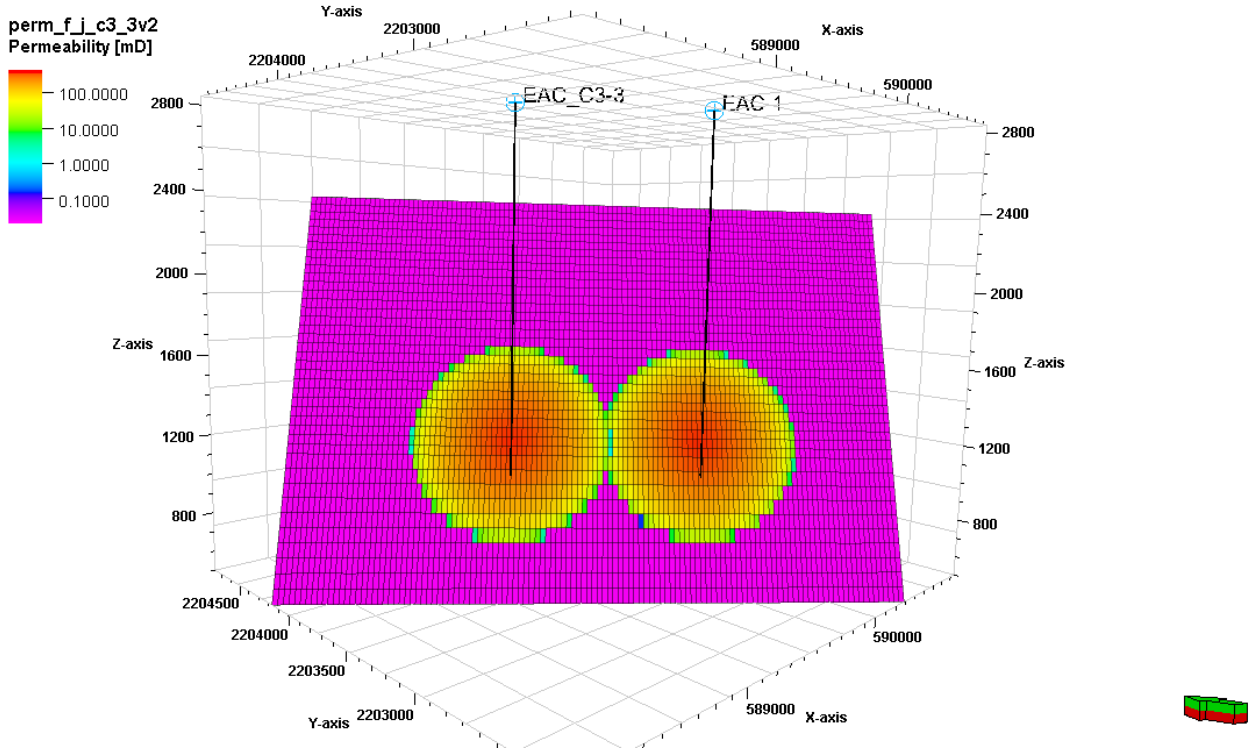

Figure 3-7. Stimulated permeability of the model used for simulation of induced seismicity with NW-trending oblique to strike-slip faults.

The second model used for induced seismicity simulation has NE-trending normal faults and is loosely based on interpretation C in Figure 2-4. The model was created to investigate what would be the risk for induced seismicity if the NE trending normal faults extend to the depth of the granites and are affected by cold water injection. Three faults with the same dip and strike were implemented in the model (Figure 3-8). The strike and dip of the faults were taken from the geological model of GEMex WP3 (D3.1; Figure 3-2). The position and extent is different from the geological model. In the model that was created here, the distance between the fault and the well is approximately 200 m at the stimulation depth (1800 mMD) (Figure 3-9). For the stimulated permeability, the same settings as in scenario 3.4 are used (Table 3-2).

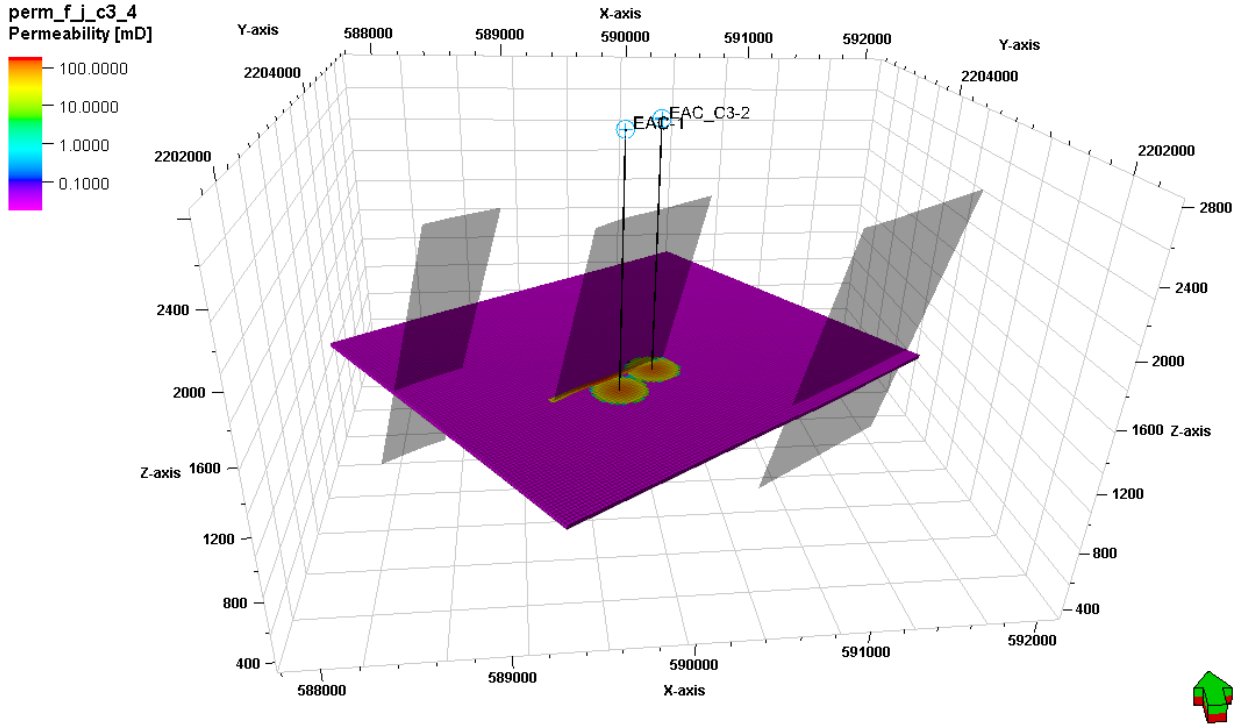

Figure 3-8. Illustration of the NE-trending normal faults used for the second model for induced seismicity simulation. One layer of the resulting model and the two wells are shown. the model is viewed from the south.

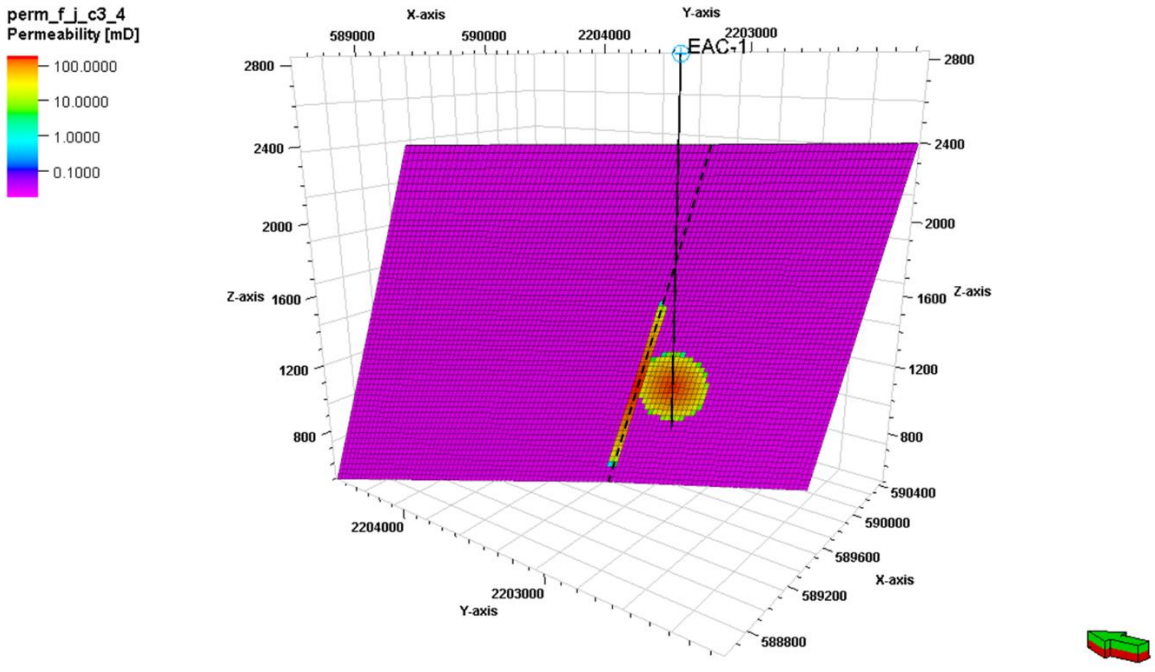

Figure 3-9. Cross section of the stimulated permeability near well EAC-1 for the model with normal faults. The dashed black line indicates the position of the fault. The black solid line is the well.

Sensitivity analysis

For the scenarios in which a fault was stimulated, a main uncertainty which was not included in the simulation approach is the fault structure: the fault was always represented by a single grid block of 25 m wide. Only the permeability and the extent of the stimulated zone were varied. To investigate the impact of the fault representation, a model was created in which the fault zone is represented in more detail. Instead of a grid spacing of 25 m, 5 m blocks were used. The permeability of the fault zone is presented in Figure 3-10. In Figure 3-10A the fault permeability is uniform across the width of the fault. In Figure 3-10B, the fault has the highest permeability near the fault core. The transmissivity of both faults is the same.

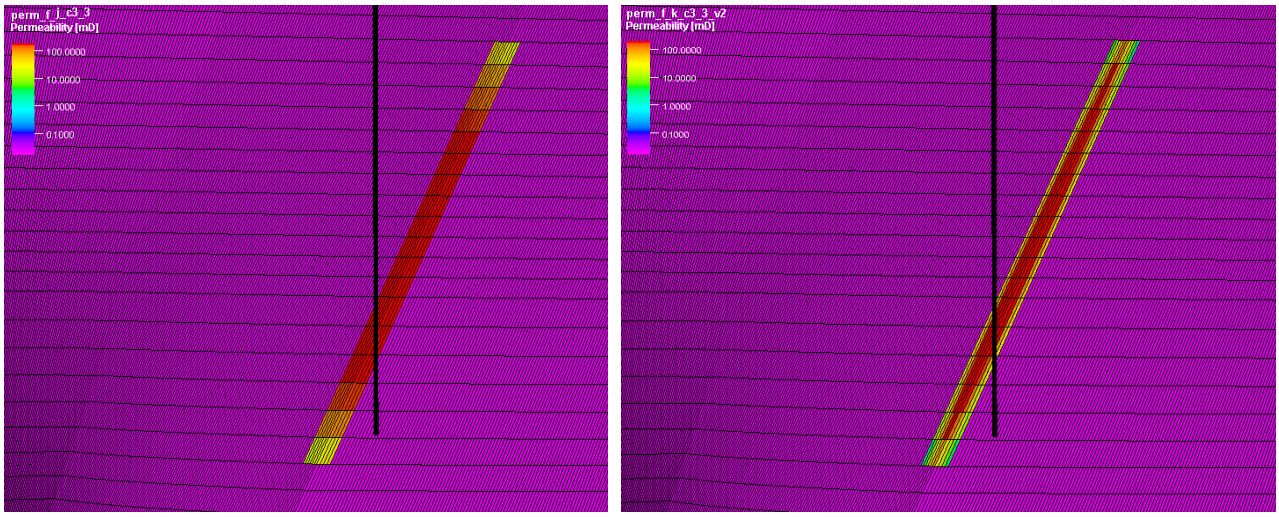

A B

Figure 3-10. Cross section of a detailed representation of the fault. A: uniform permeability across the fault zone. B: highest permeability around the fault core.

3.4.2 Reservoir model parametrization

Because of the limitation of the preliminary model from June 2019, that the surfaces are not entirely matched yet to the well tops identified in the wells, most properties of the model were taken constant over the entire model depth interval, irrespective of the layer. In Table 3-4, an overview of the input settings of the model is given (other than those relating to the stimulation which were discussed in Section 3.2). The same values were used for the box model that was used for the sensitivity analysis and induced seismicity calculations.

For the wells, no skin has been assumed. Theoretically, if a fractured medium is simulated as a porous medium, a negative skin can be used to correct for the overestimation of the pressure drop near the well due to radial flow rather than fracture flow (Bogdanov et al. 2003). Also, effects of chemical stimulation can be represented by a negative skin. On the other hand, many wells suffer from some form of near-well damage which can be represented by a positive skin. Since no information is available on the well skin, zero skin was assumed.

In D6.1 and D6.2, much detailed information on the parametrization of the rock properties is given. The simulation approach used at this stage however is too simplified to take many of these details into account. Other information, like the fluid properties are not available yet.

Table 3-4. Parametrization of the reservoir simulation models

Property	Values
Background porosity	0.005
Background permeability*	0.02 mD
Rock thermal conductivity	Limestone: 250 kJ/m/day/C
	Skarn/marbles: 336 kJ/m/day/C
	Granites: 276 kJ/m/day/C
Rock specific heat capacity	2000 kJ/m^3/C @ 20 °C
	2400 kJ/m^3/C @ 200 °C
	2600 kJ/m^3/C @ 300 °C
Fluid density	1006 kg/m^3 @ standard conditions
Fluid viscosity	1.0 cP @ 20 °C
	0.086 cP @ 300 °C
Fluid specific heat capacity	3.9 kJ/kg/C
Temperature gradient	145 °C/km
Pressure initial condition	80 bar @ 2000 m AMSL
Well diameter and completion	0 – 800 mMD: 0.17 m (6 5/8 inch) casing
	800 – TD: 0.15 m (5 7/8 inch) open hole

Boundary and initial conditions

No-flow boundary conditions were applied on all boundaries of the model. Since the unstimulated reservoir is assumed to be very tight, this is likely to be a good approximation. Also no heat exchange was assumed on the boundaries. Since the cooled area is in all scenarios quite far from the boundaries, this should also provide a good approximation. As initial conditions, hydrostatic pressure equilibrium was used and the temperature gradient as specified in Table 3-4 in combination with a surface temperature of 15 °C. It was assumed that the available pore space is initially filled with the same fluid that is injected. This simplifies the numerical simulations and has little impact on the results since the unstimulated rock volume is very tight.

Well control

Both wells were run on rate constraint in combination with a maximum cq minimum bottom hole pressure constraint. The rate was 2400 m^3/d or 3600 m^3/d for both wells depending on what can be achieved. The rate was taken lower in case of fast thermal breakthrough to delay the breakthrough. The maximum bottom hole injection pressure was set to 500 bar. Minimum production pressure was 20 bar. The pressure constraints have been set wide to allow the rate to be achieved as much as possible. In reality, these values are not reasonable.

3.4.3 Wellbore model

The dynamic subsurface model described in the previous section was used to simulate the inflow from the reservoir into the wells. To estimate the production at surface, including steam quality, the multi-feed zone geothermal wellbore simulator called HOLA was used (Bjornsson and Bodvarsson, 1987; Aunzo, 1991). The simulator calculates the pressure and temperature profile in the wellbore for different boundary conditions.

The borehole simulations were only done for three scenarios, namely stimulation of the fracture network for the three depth cases: 800 m, 1500 m and 1800 m (scenarios 1.2, 2.2 and 3.2 in Table 3-2). General input

settings are given in Table 3-5. Further input used is the rock thermal conductivity (2.50 W/m/C), rock density (2800 kg/m^3) and rock heat capacity (900 J/kg/C).

Table 3-5. Input settings used for calculation of the flow in the wellbore with HOLA.

	Length (m)	Radius (m)	Roughness (m)	Distance between simulation nodes (m)
Section 1	800	0.09	0.00005	25
Section 2	1000	0.075	0.0005	25

3.4.4 Geomechanical input

As discussed in the geological input (Section 3.4.1), two cases are considered for the analysis of the stresses and induced seismicity:

- One reservoir model where the pre-existing faults are NW-trending oblique to strike-slip faults; referred in the following as the strike-slip fault model and very similar to scenario 3.3,
- One reservoir model where the pre-existing faults are NE-trending, normal-slip faults; referred in the following as the normal-slip fault model.

To simulate induced stresses and induced seismicity, 20 years of production were simulated for a doublet identical to the setup for the heat production scenarios. Re-injection was again done at 50 °C. Input settings for the reservoir simulation are listed in Table 3-4.

The thermal expansion coefficient was kept constant at 3x10^{-5} K^{-1} for all the simulations presented in this report. Two types of in-situ stresses were used. For the strike-slip fault model a strike-slip faulting regime was assumed with a minimum horizontal stress gradient of 19.2 MPa/km, a vertical stress gradient of 24.3 MPa/km, and a maximum horizontal stress gradient of 34.4 MPa/km with an orientation N056E (Kruszewski et al., 2020 in review). For the normal-slip fault model, a normal-slip faulting regime was assumed with a minimum horizontal stress gradient of 19.2 MPa/km, a vertical stress gradient of 29 MPa/km, and a maximum horizontal stress gradient of 27 MPa/km with an orientation N056E. For both faulting regimes the pore pressure gradient was 8.73 MPa/km.

In terms of base case scenario, we assumed for the frictional parameters of the Dieterich's seismicity rate theory, that A=0.005 (eq. 2). The background stressing rate was taken as $\dot{S}_0$ of 0.001 MPa/year, representative for a stress drop of 1 MPa every 1000 years along the faults of interest. Consequently, for our base case scenario, the characteristic time delay T_a is roughly 50 years.

4 Production results

4.1 Heat production for development scenarios

4.1.1 Downhole conditions

For evaluation of the performance and resource sustainability, three key performance indicators at downhole conditions are used which are:

- initial production temperature
- average heat produced *H* at downhole pressure and temperature (averaged over 20 years)

$$H = \frac{1}{n}\sum_{i=1}^{n} Q_i(BHT_{prod}(t_i) - BHT_{inj}(t_i))$$

Where

Q production rate

BHT Bottom Hole Temperature

- Average pressure difference between injector and producer (averaged over 20 years).

The reinjection temperature is set to 50°C for all scenarios. For the higher temperature scenarios this is likely to be unrealistically low. However, the shallow scenarios have such a low production temperature, that a low value needed to be selected. To characterize the scenarios, also the stimulated volume is presented.

In Table 4-1, the results of the three performance indicators defined above are presented for all 15 development scenarios. For some scenarios, no results are presented. This is for different reasons:

- For scenarios 1.1b, 1.3 and 1.4, the stimulated area propagates into the volcanites. This does not result in a sensible production scenario because at this shallow depth, temperature is too low.
- For scenario 2.3, there was no suitable fault crossing the well at an appropriate depth.

The results of these scenarios should be interpreted with extreme caution since the uncertainty is very high, which is not well represented by the standard deviation. Because only a limited number of uncertainties has been taken into account in this analysis, the standard deviation in Table 4-1 does not represent the real uncertainty. Mainly the trends in the results are interpreted rather than the absolute numbers. From the overview of the results it is clear that the scenarios in which a fracture network is stimulated shows the highest amount of heat produced and largest stimulated rock volume. In terms of initial temperature, the difference between the scenarios at a single depth is not very large, since uncertainty in the pre-production temperature is not taken into account.

In the last column, the average pressure difference between the injector and producer is listed for the given rate. These values are difficult to interpret because even more than the other values, these depend on the chosen permeability. What can be seen from the results, is that a low required pressure/high permeability such as for scenario 3.1b is not necessarily beneficial for the produced heat due to short circuiting between injector and producer.

Table 4-1. Overview of the performance indicators at downhole conditions for all development scenarios. The average and standard deviation (between brackets) of the 50 realisations are given.

Sc number	Stimulation depth (m DM)	stimulation concept	Stim. Rock volume* (m^3)	Initial T (°C)	Average prod. heat (MW)	Average delta P (bar) @ given rate
1.1a	800	Hydraulic fracture (height constrained)	5.1×10^5 (1.7×10^5)	136 (1)	3.2 (0.8)	119 (44) @ 2400 sm^3/d
1.1b	800	Hydraulic fracture (unconstrained)	Too shallow			
1.2	800	Stimulated fracture network	3.9×10^7 (2.6×10^7)	132 (1)	7.1 (1.5)	112 (20) @ 2400 sm^3/d
1.3	800	Reactivated fault	Too shallow			
1.4	800	combination	Too shallow			

2.1a	1500	Hydraulic fracture (height constrained)	5.0×10^5 (1.8×10^5)	226 (1.5)	6.5 (1.5)	102 (43) @ 2400 sm^3/d
2.1b	1500	Hydraulic fracture (unconstrained)	5.7×10^5 (1.8×10^5)	218 (2)	5.9 (1.2)	13.6 (3.3) @ 2400 sm^3/d
2.2	1500	Stimulated fracture network	3.9×10^7 (2.6×10^7)	219 (4)	22.1 (5.5)	90 (29) @ 3600 sm^3/d
2.3	1500	Reactivated fault	No fault crossing the wells at appr. this depth			
2.4	1500	combination	5.9×10^7 (2.6×10^7)	218 (6)	24 (5)	89 (36) @ 3600 sm^3/d
3.1a	1800	Hydraulic fracture (height constrained)	5.1×10^5 (1.9×10^5)	267 (2)	7.5 (2)	92 (46) @ 2400 sm^3/d
3.1b	1800	Hydraulic fracture (unconstrained)	5.6×10^5 (1.7×10^5)	258 (3)	7.5 (1.5)	12.4 (3.5) @ 2400 sm^3/d
3.2	1800	Stimulated fracture network	3.9×10^7 (2.6×10^7)	261 (3)	28.3 (7.5)	73 (23) @ 3600 sm^3/d
3.3	1800	Reactivated fault	4.2×10^7 (2.0×10^7)	261 (1)	22.1 (3.5)	92 (23) @ 2400 sm^3/d
3.4	1800	combination	5.9×10^7 (2.8×10^7)	260 (3)	30.8 (6.6)	67 (26) @ 3600 sm^3/d

* stimulated volume per well (not taking into account overlap between stimulated areas of two wells)

In the following, the results per development scenario are discussed in more detail.

Hydraulic fracture scenarios

The average produced heat is presented as a function of fracture half length (Figure 4-1), fracture half height (Figure 4-2) and stimulated rock volume (Figure 4-3). The average produced heat strongly depends on stimulated rock volume (Figure 4-3). Fracture length has a larger impact on the total heat produced than fracture height (Figure 4-1 versus Figure 4-2). The thermal breakthrough is very fast for all scenarios due to the small stimulated volume. In Figure 4-4 and Figure 4-5, the production temperature is given for all realizations for scenario 2.1a and 2.1b as an example. Thermal breakthrough is very similar for the other scenarios.

The average produced heat for the scenarios in which the vertical fracture growth is limited (a-scenarios) is similar compared to the scenarios in which the vertical growth is not limited (b-scenarios) (Figure 4-1 to Figure 4-3). This is because the stimulated rock volume for both types of scenarios is very similar despite the difference in fracture dimensions (Figure 4-3).

If the created hydraulic fractures can intersect a permeable natural fracture network or fault damage zone, of course the results may be much better.

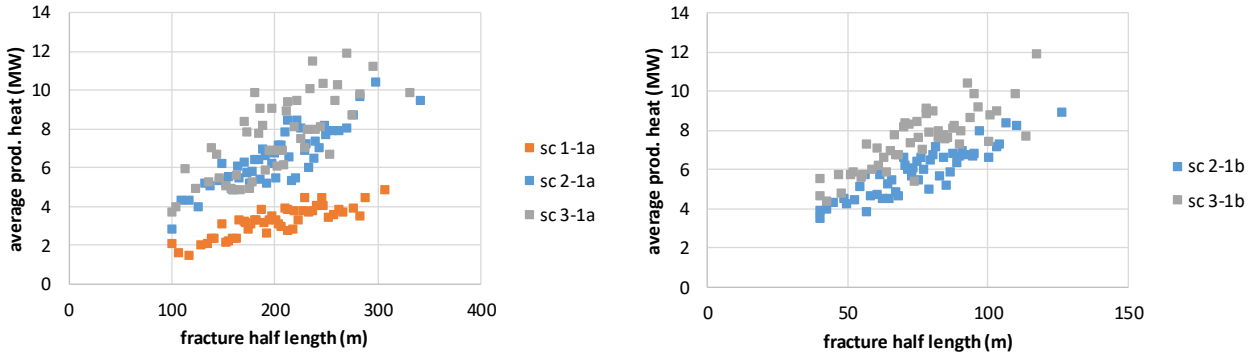

Figure 4-1. Average produced heat H as a function of the half length of the hydraulic fracture. Every square represents one realization (left: fracture with constrained height; right: fracture with unconstrained height).

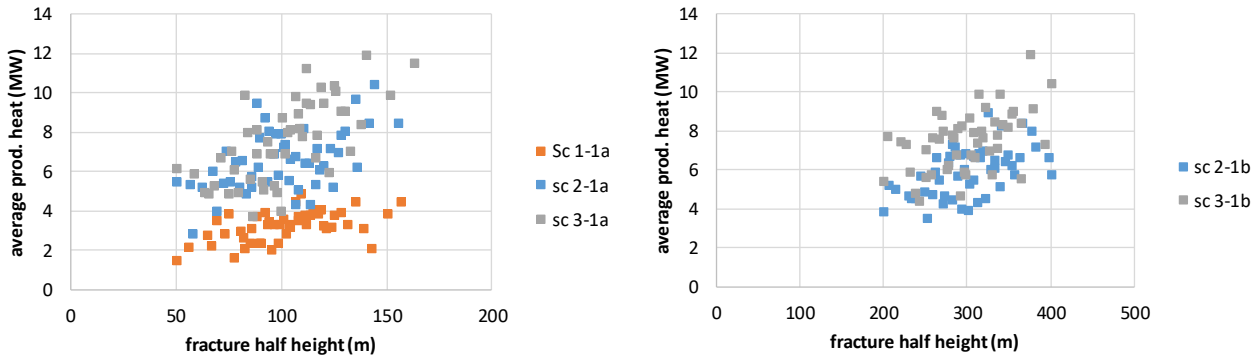

Figure 4-2. Average produced heat H as a function of the half height of the hydraulic fracture. Every square represents one realization (left: fracture with constrained height; right: fracture with unconstrained height).

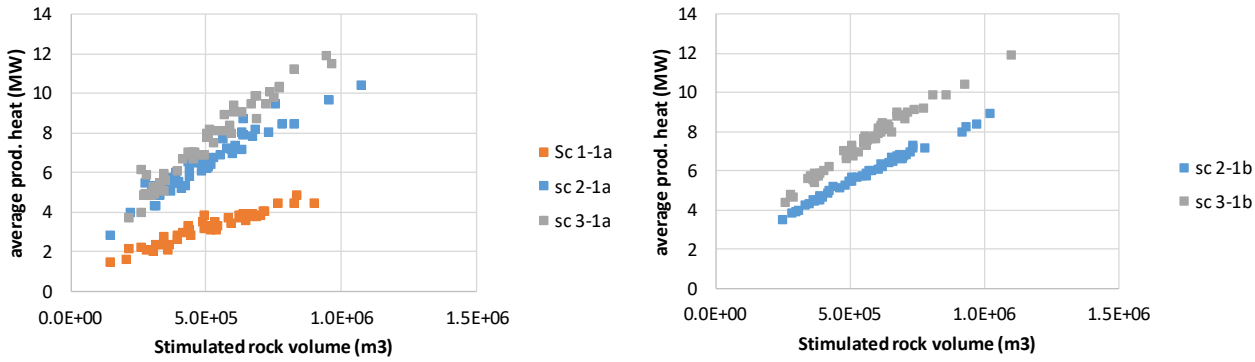

Figure 4-3. Average produced heat H as a function of the stimulated rock volume. Every square represents one realization (left: fracture with constrained height; right: fracture with unconstrained height).

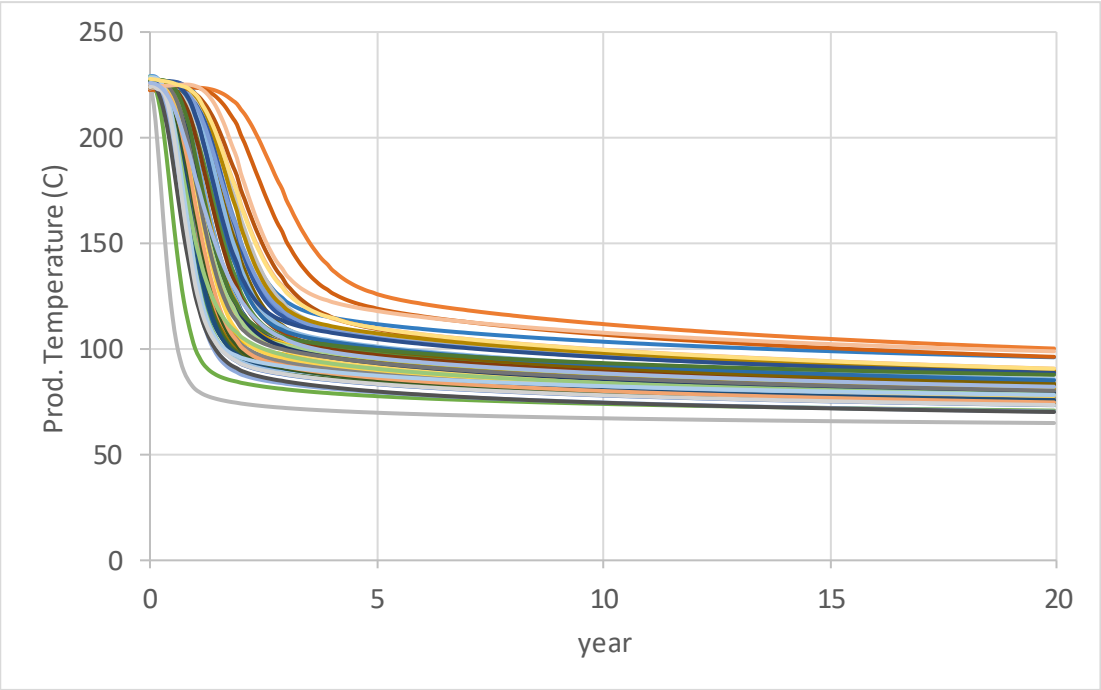

Figure 4-4. Production temperature for 20 years for scenario 2.1a for all 50 realisations. Every line represents one realisation.

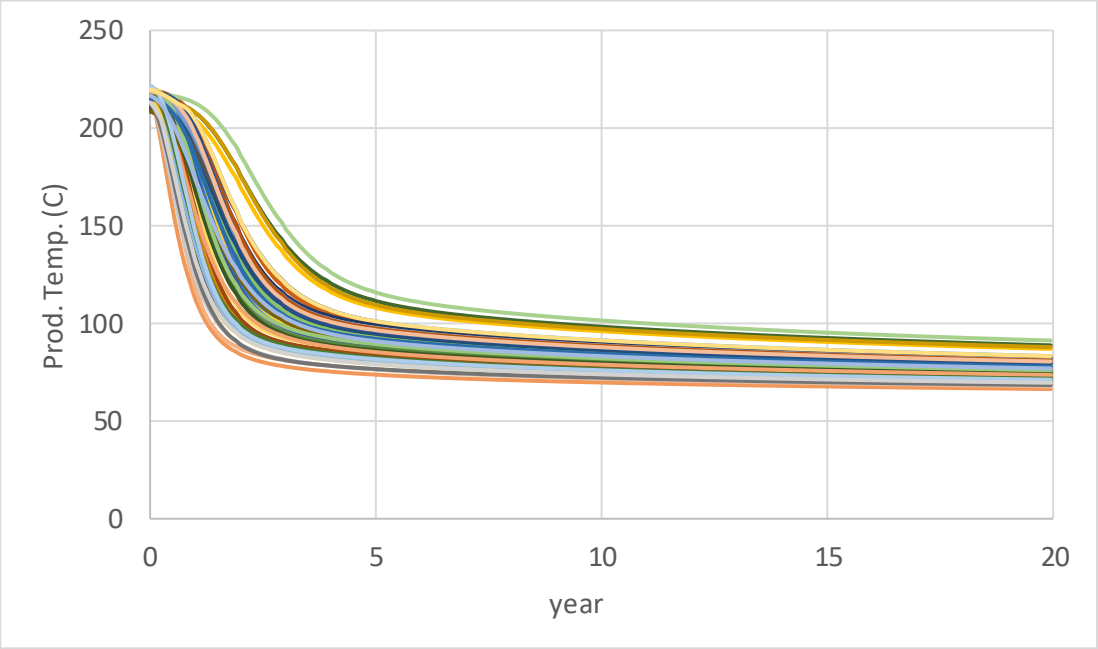

Figure 4-5. Production temperature for 20 years for scenario 2.1b for all 50 realisations. Every line represents one realisation.

Stimulated fracture network scenarios

The stimulated fracture network generally has the best results in terms of produced heat (compare Figure 4-6 with Figure 4-1 to Figure 4-3), because the volume of stimulated rock is the largest. This reduces thermal breakthrough compared to scenarios in which only a thin zone is stimulated (hydraulic fracture and

reactivated fault) (Figure 4-7 and Figure 4-8 compared to Figure 4-5). The range in thermal breakthrough is very large and depends mainly on the size of the stimulated area (Figure 4-6). This scenario is the most desirable in terms of production, but also the least likely to be achievable.

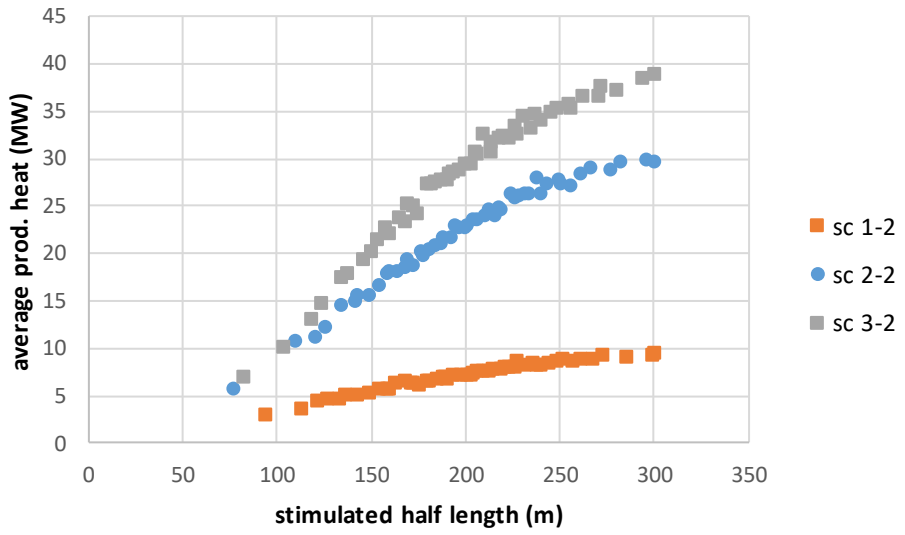

Figure 4-6. Average produced heat H as a function of the half length of the stimulated area.

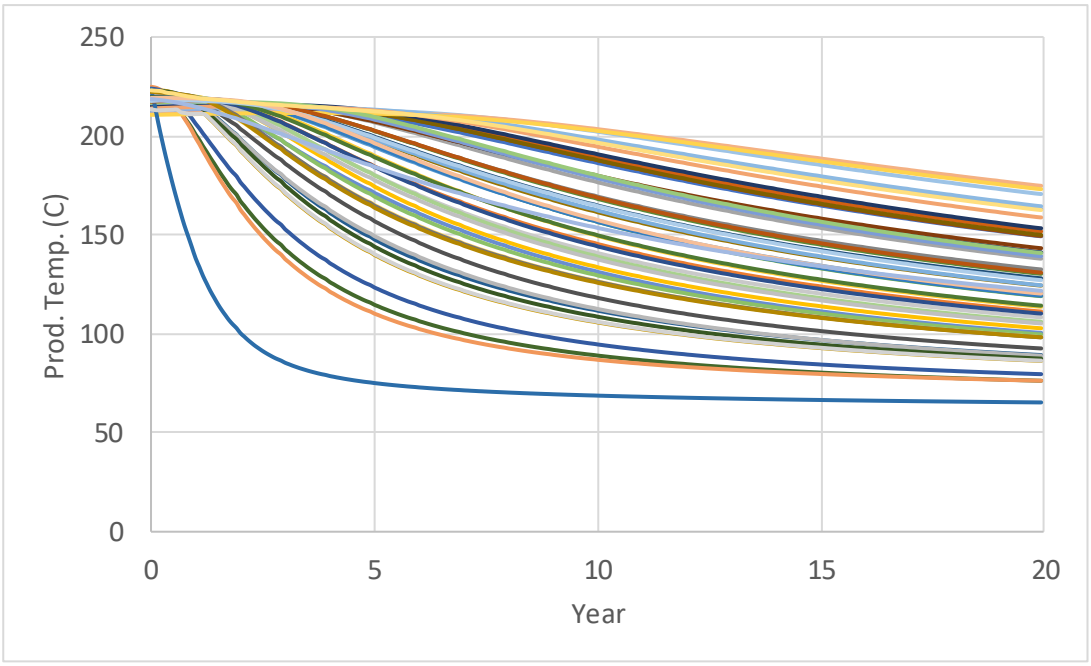

Figure 4-7. Production temperature for 20 years for scenario 2.2 for all 50 realisations. Every line represents one realisation.

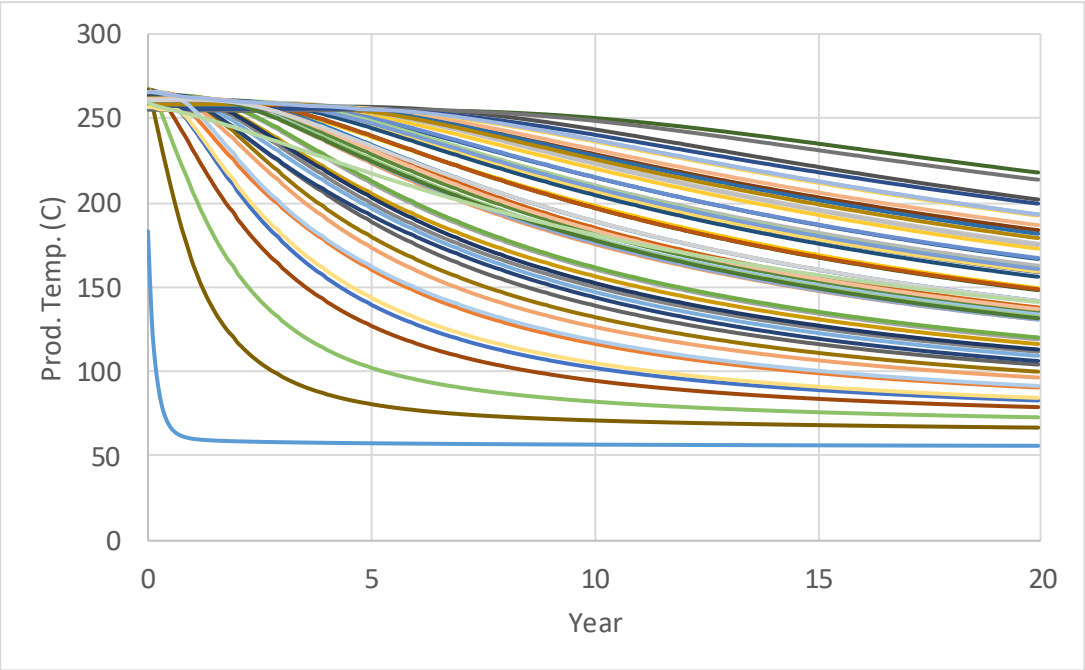

Figure 4-8. Production temperature for 20 years for scenario 3.2 for all 50 realisations. Every line represents one realisation.

Stimulated fault scenarios

In Figure 4-9, the average produced heat for the stimulated fault zone scenario (scenario 3.3) is compared to the other scenarios at this depth. For the stimulated fault, the range in stimulated length was much larger than for the other scenarios. In particular the hydraulic fracture scenarios have a much smaller range. The reason for selecting larger stimulated length for the fault is that it is assumed that if a pre-existing fault is reactivated, a larger part is reactivated than in case a tensile fracture needs to be created. Due to the large size of the stimulated area, thermal breakthrough is not very fast (Figure 4-11 and Figure 4-12). Figure 4-12 shows the temperature in the reservoir after 20 years of production and injection for a half length of 500 m. On the other hand, the achieved production rate is low, because the transmissivity is low due to the assumed small width of the stimulated zone (25 m, see Figure 3-5 for illustration of the stimulated zone). The stimulated rock volume (Figure 4-10) is in the same range as for scenario 3.2 and 3.4, but due to the lower rate, the heat production is lower.

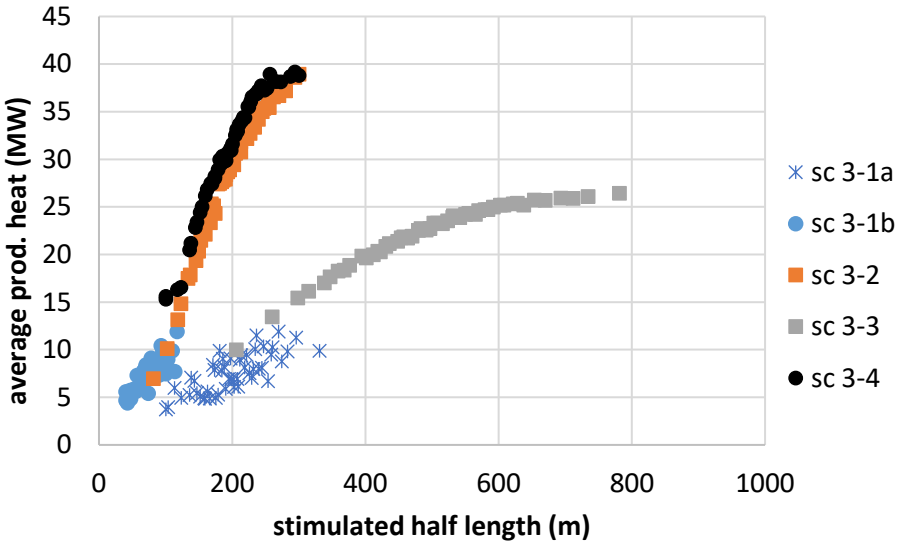

Figure 4-9. Average produced heat H as a function of the half length of the stimulated area for all scenarios at a depth of 1800 m.

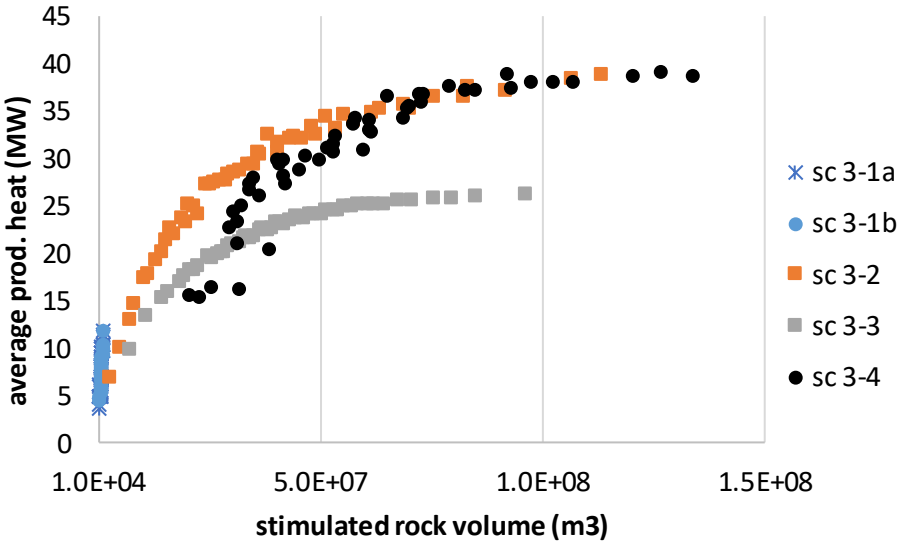

Figure 4-10. Average produced heat H as a function of the stimulated rock volume for all scenarios at a depth of 1800 m.

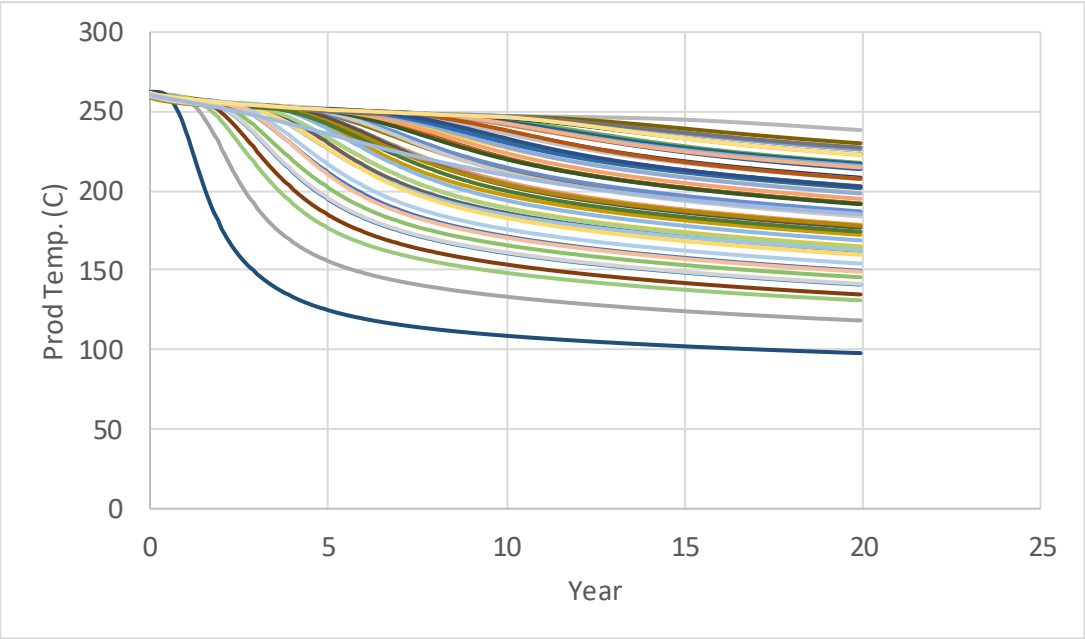

Figure 4-11. Production temperature for 20 years for scenario 3.3 for all 50 realisations. Every line represents one realisation.

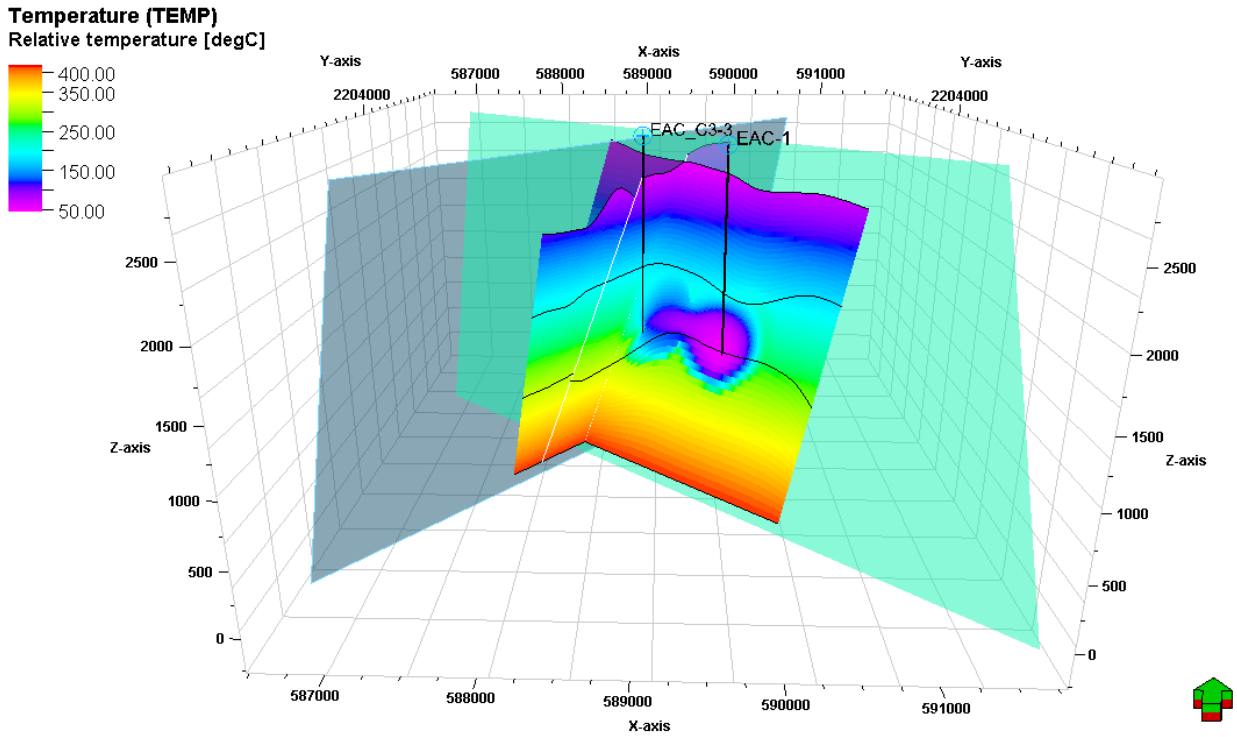

Figure 4-12. Illustration of the temperature after 20 years of injection in EAC-1 for the base case (averages from Table 3-4). Black thin lines indicate the surfaces between formations, white lines indicate the fault positions and the vertical black line are the well bores.

Combination scenario

The results of the combination scenarios are very similar to the scenarios in which the fracture network only is stimulated (Figure 4-13, Figure 4-9, Table 4-1). As long as the stimulated fault zone has sufficient cross-fault permeability, the impact on the production performance is limited.

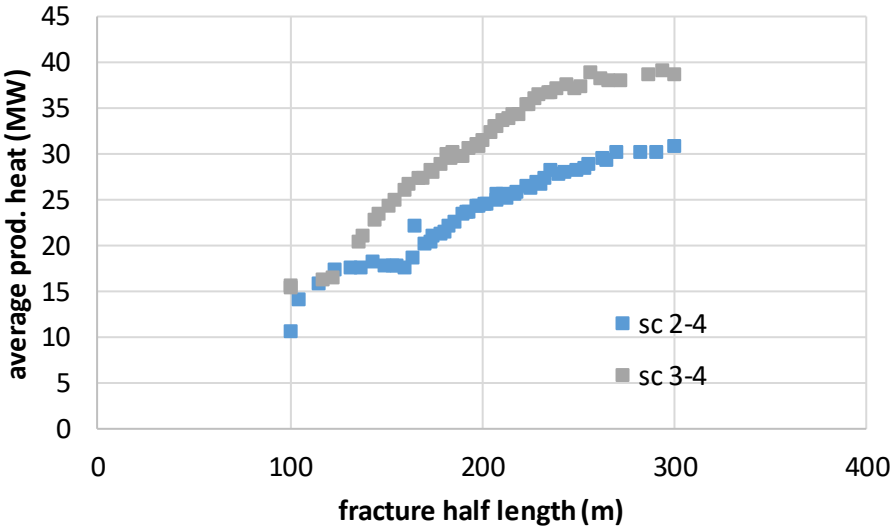

Figure 4-13. Average produced heat H as a function of the half length of the stimulated fracture network for the two combination scenarios 2-4 and 3-4.

4.1.2 Surface conditions

Based on the results at downhole conditions, the average results of the scenarios 1.2, 2.2 and 3.2 are translated to surface conditions. In Table 4-2, the inputs for the well model are listed. They are based on the average case of each of the scenarios. The average case is simulated separately by using the averages of the probability distributions. The results are presented for steady state conditions.

Table 4-2. Input settings at downhole conditions for the calculation of surface conditions using HOLA.

Scenario	Depth of stimulation	Temperature T (°C)	Density ρ (kg/m^3)	Rate Q_m (kg/s)	Enthalpy (kJ/kg)	Viscosity μ (cP)	PI* (m^3)
Sc 1.2	800 m	134	940	26.1	568	0.2	1.5 x 10^{-12}
Sc 2.2	1500 m	221	850	35.4	950	0.12	2.8 x 10^{-12}
Sc 3.2	1800 m	262	800	33.3	1130	0.1	3.5 x 10^{-12}

* Productivity Index defined as ($\mu Q_m / \rho \Delta P$)

In Figure 4-14, the pressure and temperature in the wells are presented. For Sc 1.2, the pressure was too low to lift the fluids out of the well. The main reason for this was the low bottom hole pressure resulting from the low Productivity Index (PI). The low PI is the result of the assumption that the stimulation of the fracture network occurs in all directions. This means that part of the fractures are hidden behind the casing. The inflow into the well thus has to occur through a very small part of the well. For Sc 2.2, the rate of 35.4 kg/s reaches the surface at 13 bar, 191 °C, and 4.4% dryness. For Sc 3.2, the flow rate at surface was 33.3 kg/s at 28 bar, 229 °C and 4% dryness.

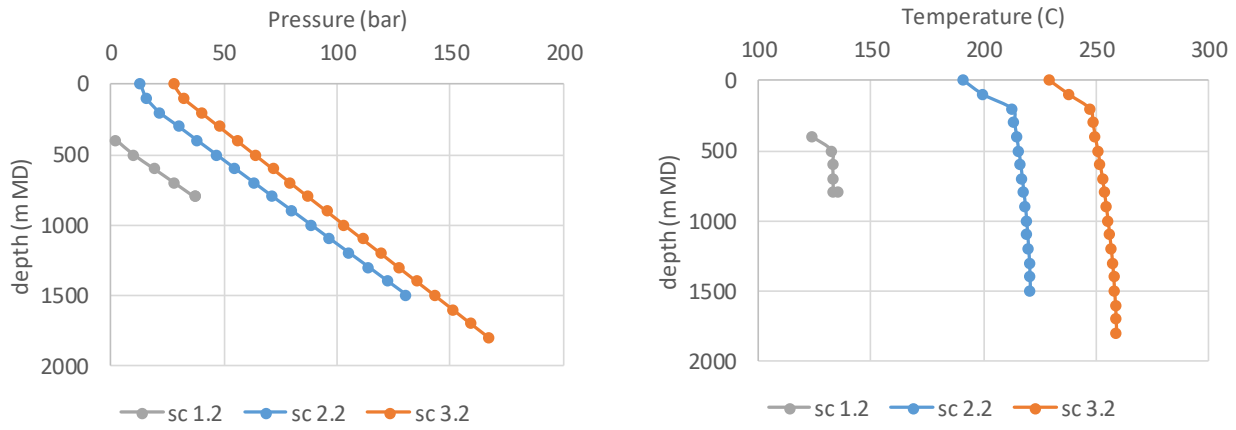

Figure 4-14. Pressure (left) and temperature (right) versus depth for scenarios 1.2, 2.2 and 3.2.

One of the options for stimulation includes installing a casing to the desired depth. The 5 7/8" to 6" open hole diameter allows to install a casing with maximum outer diameter of 4 ½" and maximum inner diameter of ~4". To evaluate the impact of the additional pressure drop, scenario 3.2 was rerun with a completion with 0.05 m radius and 0.00005 m roughness over the entire depth. For the same flow rate of 33.3 kg/s, the well head pressure reduces to 24 bar, temperature reduces to 222 °C and dryness increases to 6.3%. For this rate, the impact of the smaller casing is limited, also because the casing is expected to be less rough than the original open hole.

4.2 Sensitivity analysis

The representation of the fault zone has a large impact on the results. The first sensitivity is for the width of the fault zone. For this sensitivity analysis, the same model is used as in Section 4.1, scenario 3.3. In Figure 4-15 the production temperature is shown for two runs in which only the width of the fault zone is varied. As can be seen from the results this has a large impact on the thermal breakthrough: the stimulated rock volume of the 50 m wide fault zone is twice as large.

In Figure 4-16, the numerical representation of the fault is more detailed (see Figure 3-10). The coarse grid and the fine grid with constant permeability *k* only differ in the grid representation. The difference in cold water breakthrough is small. In the fine grid representation in which the permeability is higher near the fault core (variable *k*), the water breakthrough starts earlier, because the cold front is less uniform. However, both effects are smaller than the impact of the uncertainty on the fault zone in Figure 4-15.

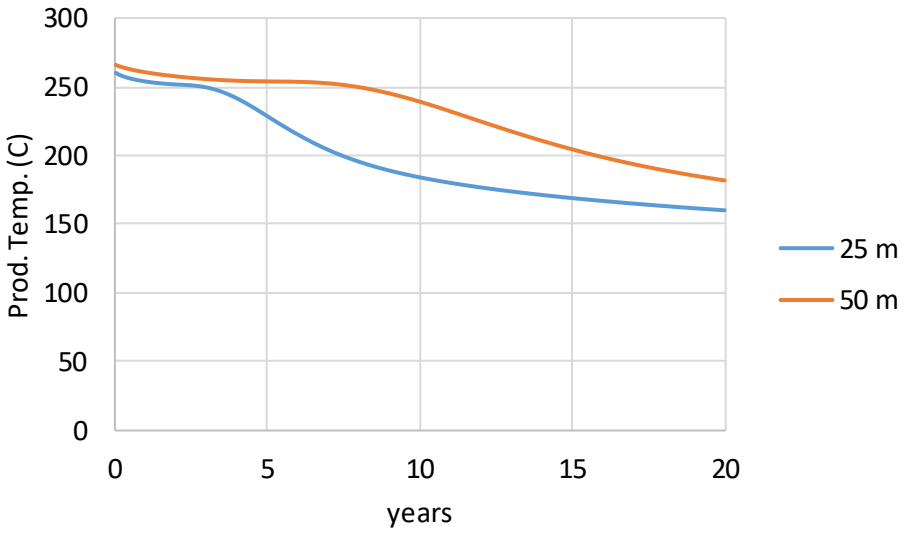

Figure 4-15. Production temperature for the scenario 3.3 with a 25 m and 50 m wide fault zone.

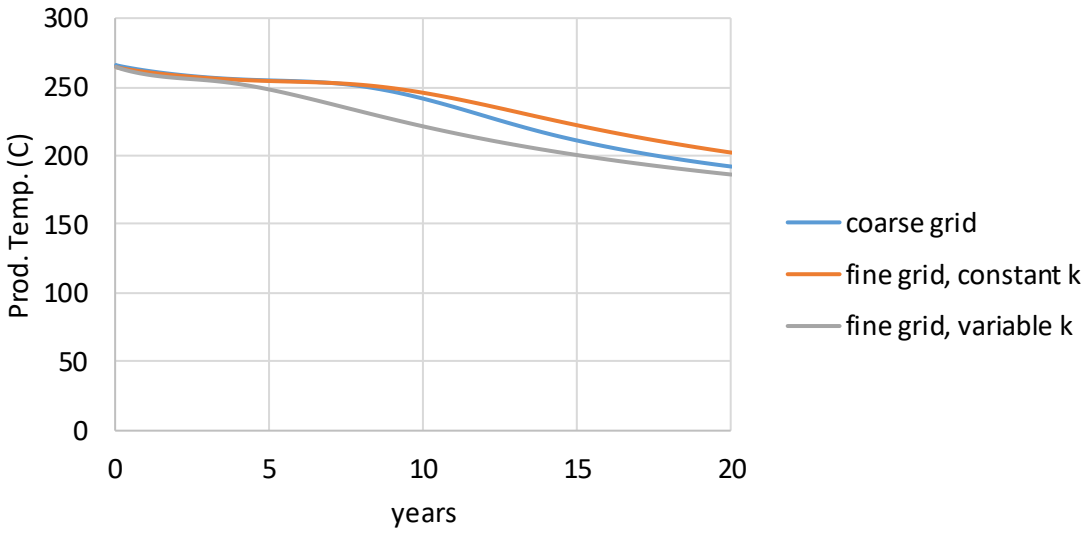

Figure 4-16. Production temperature for the scenario 3.3 (box grid), with the fault represented with a coarse grid, the same fault but represented with a fine grid with 5 m wide blocks and a fault represented with a fine grid with variable *k* illustrated in (Figure 3-10).

5 Induced seismicity results

5.1 Results pressure and temperature

To simulate induced stresses and induced seismicity, 20 years of production was simulated for a doublet (period 2019 - 2039). Re-injection was done at 50 °C. Figure 5-1 shows the pressure for the strike-slip faults after 20 years. Figure 5-2 shows the temperature at the same time. Figure 5-3 shows pressure and temperature for the model with NE-trending normal faults after 20 years of injection.

Even if both models (the strike-slip fault model and the normal-slip fault model) include multiple faults, for each model, results of MACRIS are only presented for one single fault where the changes in pressure and temperature are significant – for the other faults these changes are minor.

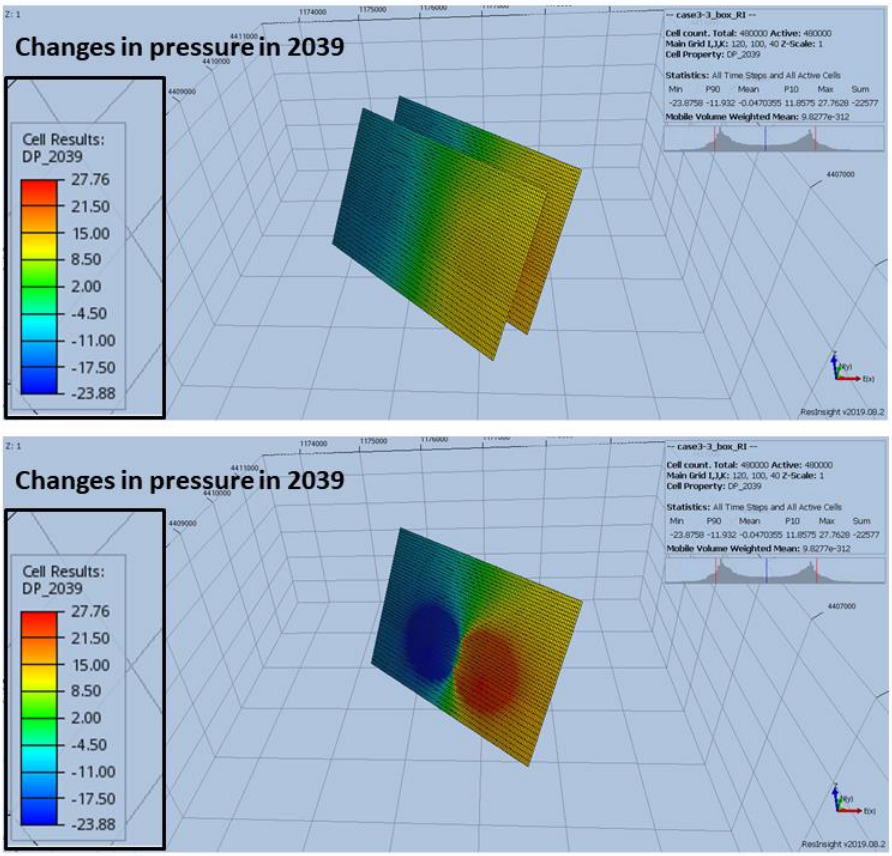

Figure 5-1. Strike-slip fault model: changes in fault pressure (top: both faults, bottom: fault used in this analysis).

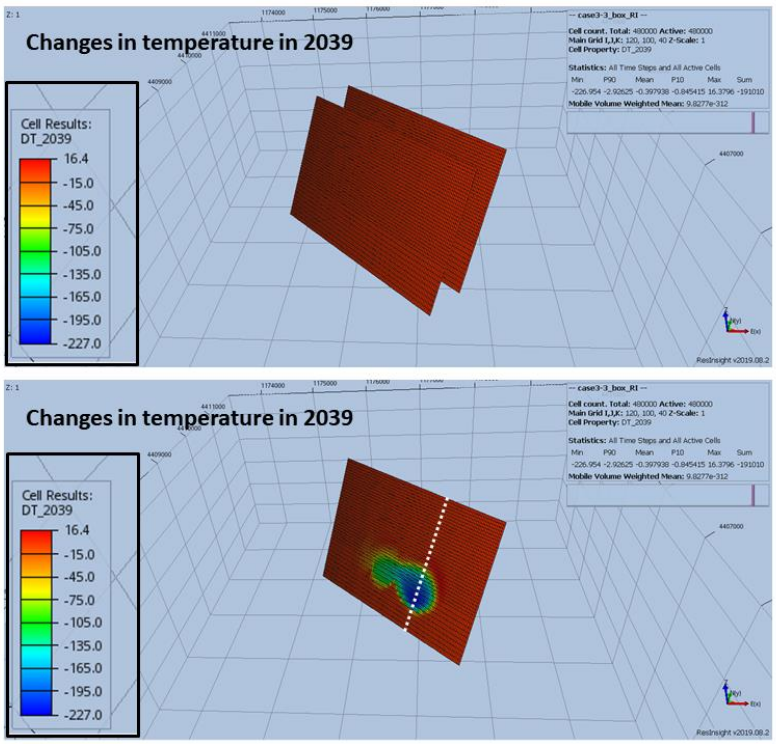

Figure 5-2. Strike-slip fault model: changes in fault temperature. The sub-vertical dashed white line indicates the pillar where the changes in Coulomb stress, pressure, temperature are presented in Figure 5-4 (top: both faults, bottom: fault used in this analysis).

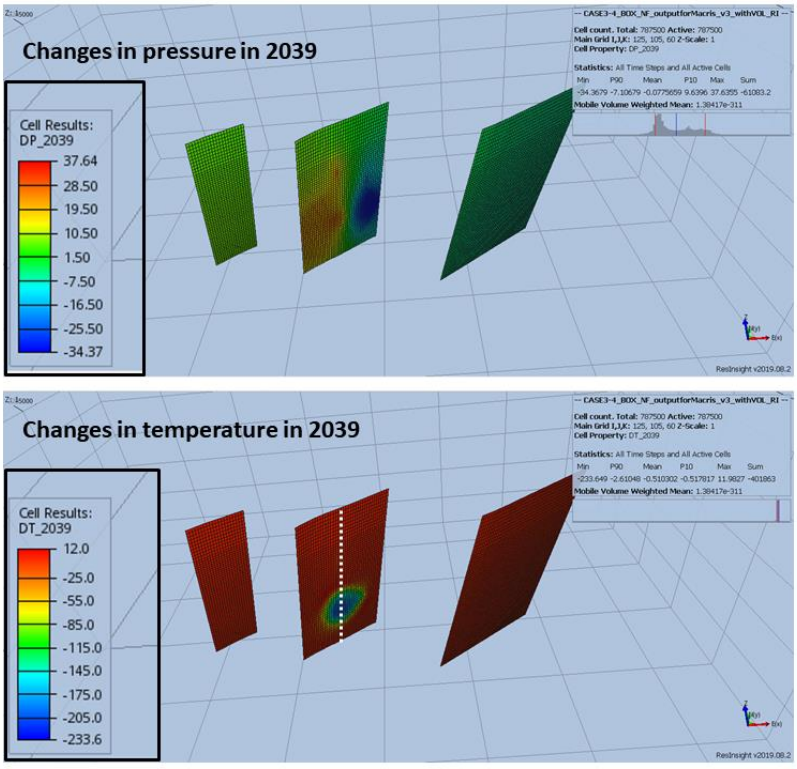

Figure 5-3. Normal-slip fault model: changes in fault pressure (up) and temperature (down). The sub-vertical dashed white line indicates the pillar where the changes in Coulomb stress, pressure, temperature are presented in Figure 5-5.

5.2 Results stress

Figure 5-4 and Figure 5-5 present the temporal evolution of the changes in fault temperature, fault pressure, and Coulomb stress (eq. 1) for respectively the strike-slip fault model and the normal-slip fault model. Note here that in all the figures of this section the depth is given as the depth relative to the top of the reservoir simulation model which is at 2400 m AMSL. When the changes in Coulomb stress is positive, the fault is following a destabilizing stress path and can eventually reach the failure line.

The changes in fault temperature, fault pressure, and Coulomb stress are displayed along the fault pillars (see Figure 5-2 and Figure 5-3) where the maximum changes in temperature are computed. For both models, the stress changes in the fault due to pressurization are much smaller than the ones due to cooling. The changes in Coulomb stress are significantly higher for the normal-slip model than for the strike-slip fault model – even if the magnitude of the changes in fault pressure and temperature are similar. Only in the case of the normal-slip fault model, the positive changes in Coulomb stress surpass the failure line. If the Coulomb failure criterion would dictate fault reactivation, this would only occur on the faults of the normal-slip fault model.

For both the strike-slip fault model and the normal-slip fault model, the maximum change in fault temperature and Coulomb stress are observed roughly at a depth of -1500 m. These maximum changes are not reached at the end of the model simulation, that is 2039 years (i.e. 20 years after the start of circulation-production). Indeed, the maximum change in temperature (that is the cold front of 50 °C) at a depth of -1500m reaches the strike-slip fault already 0.5 year after the start of circulation-production; it takes about 3 years for the normal fault. After that the cold front of 50 °C reaches the fault at the depth of -1500m, the temperature change remains constant at this location and the cold front progressively spreads out laterally along the fault over time. As a result, the Coulomb stress change follows an “annular-type” spatio-temporal progression along the fault plane. Indeed, at the fault locations where the fault temperature remains at 50 °C (at -1500m), the Coulomb stress change starts to progressively decrease over time. While instead at the margin of this cold-centre (at -1500m), one can observe a ring of increase of the Coulomb stress change caused by the progressive cooling of the fault at these locations.

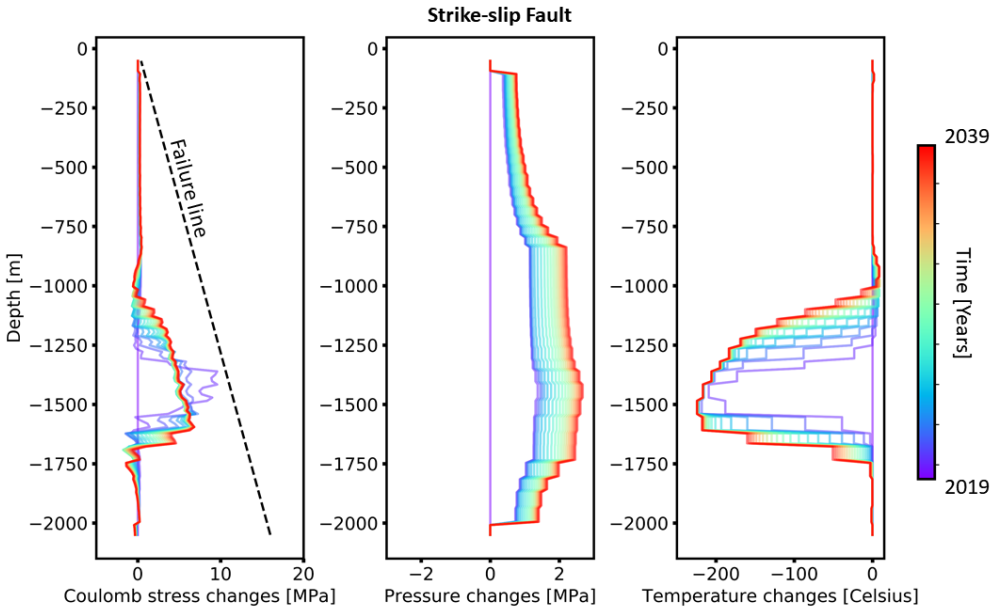

Figure 5-4. Strike-slip fault model: temporal evolution of Coulomb stress, pressure, temperature changes along the pillar presented in Figure 5-2

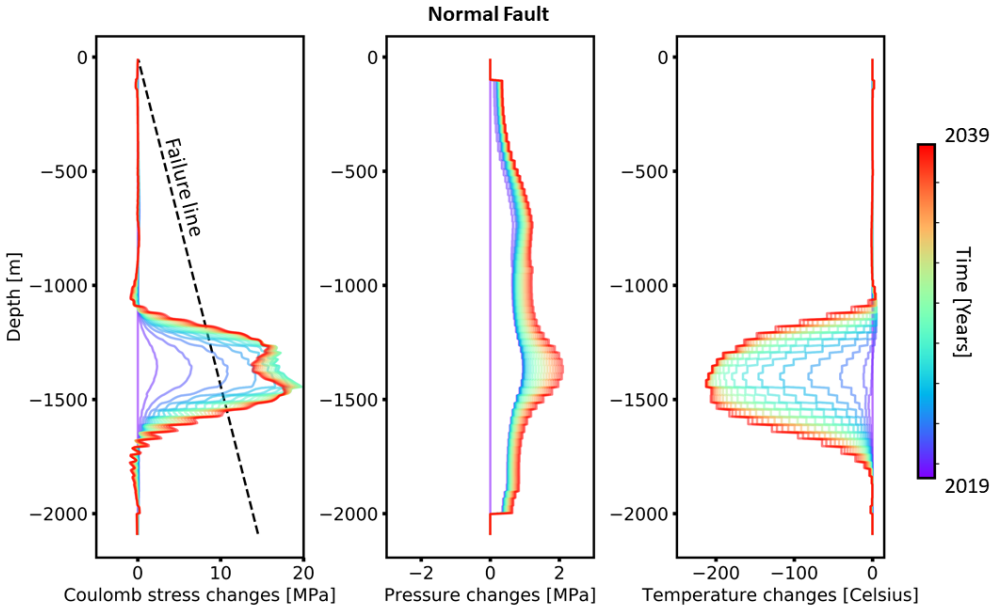

Figure 5-5. Normal-slip fault model: temporal evolution of Coulomb stress, pressure, temperature changes along the pillar presented in Figure 5-3.

5.3 Results induced seismicity

Figure 5-6 and Figure 5-7 display the inputs to the Dieterich's seismicity rate theory respectively for the Strike-slip fault model and the Normal-slip fault model. More specifically, the shear and normal stress, and

their combination (the Coulomb stress rate) are displayed at the location of the maximum change in fault temperature. Note here the Coulomb stress rate promptly decreases for the strike-slip fault model; instead for the normal-slip fault model, the Coulomb stress rate first increases and then progressively decreases.

The seismicity rate calculated with Dieterich's theory will vanish when the Coulomb stress rate drops below zero. Consequently, the strike-slip fault model shows induced events even while the Coulomb failure model doesn't, since the Coulomb stress changes are not large enough to overreach the failure line (see Figure 5-4).

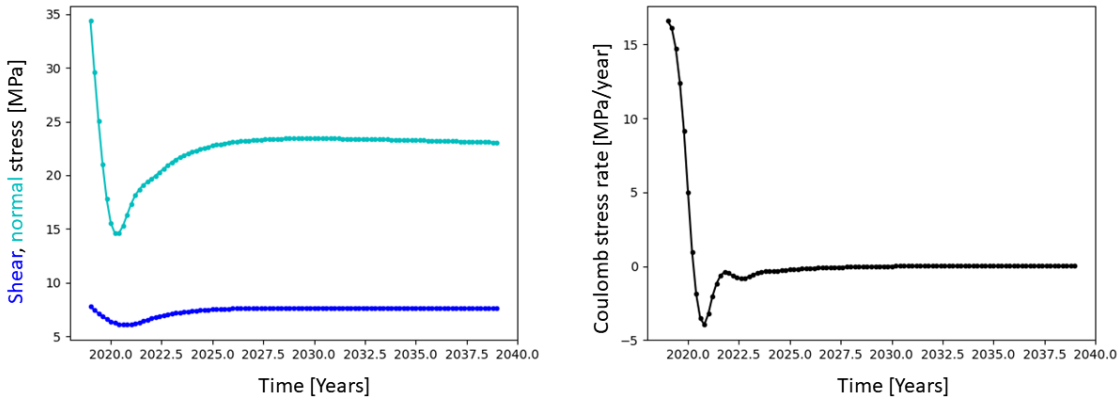

Figure 5-6. Strike-slip fault model: temporal evolution of shear, normal stress (left) and Coulomb stress rate (right) at the location of the maximum change in temperature along the fault pillar in Figure 5-2.

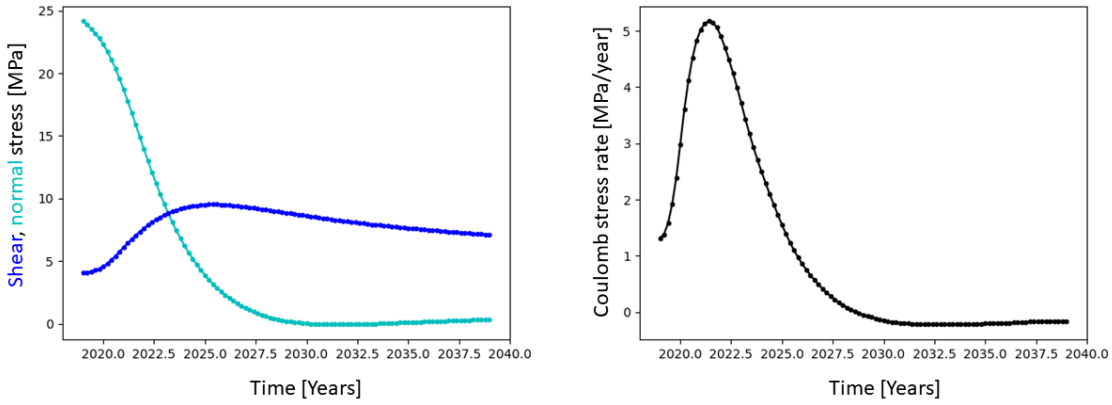

Figure 5-7. Normal-slip fault model: temporal evolution of shear, normal stress (left) and Coulomb stress rate (right) at the location of the maximum change in temperature along the fault pillar in Figure 5-3.

Figure 5-8 presents the relative seismicity rate at the location of the maximum change in fault temperature. For the base case scenario, that is $T_a = 50\ years$, the relative seismicity rate profiles almost mimic the trend of the Coulomb stress rates in Figure 5-6 and Figure 5-7. Indeed, for the strike-slip model, the relative seismicity rate promptly reaches a large maximum (R=16000) and then suddenly declines. For the normal-slip model, the increase in the relative seismicity rate is more gradual and its maximum is moderate (R=5000); also, the decline is slow, keeping the seismicity rate relatively high over a significant period.

The sensitivity of the relative seismicity rate to the T_a is also illustrated in Figure 5-8. Decreasing T_a to 5 years gives a similar seismicity rate compared to the base case scenario for both the strike-slip and normal-slip models. When increasing the characteristic delay T_a to 500 years, the sharp peak in the seismicity rate

observed for the strike-slip model almost vanishes. For the normal-slip model, the peak is delayed in time but still persists.

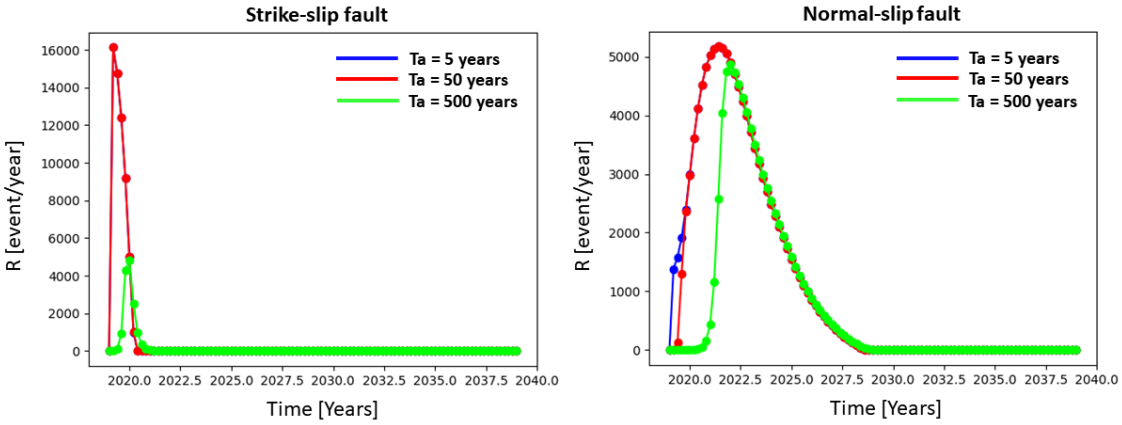

Figure 5-8. Temporal evolution of relative seismicity rate R at the location of the maximum change in temperature along the fault pillar in Figure 5-2 (left) and Figure 5-3 (right).

The spatio-temporal evolution of the relative seismicity along the fault planes is presented in Figure 5-9 and Figure 5-10 for respectively the strike-slip fault model and normal-slip fault model. The figures show the progression in time and space of the peak of relative seismicity rate. They confirm that the induced seismicity is more localized in time and less severe for the strike-slip model than for the normal-slip model. The "annular-type" spatio-temporal progression of the Coulomb stress change (as described earlier) is propagated to the spatio-temporal progression of the relative seismicity rate. At a depth of roughly -1500m where the cold front of 50 °C reaches the fault promptly, the relative seismicity rate also peaks early and then it decreases progressively. While instead, at the margin of this cold-centre (at ~ -1500m), a ring of increase of the relative seismicity rate is observed.

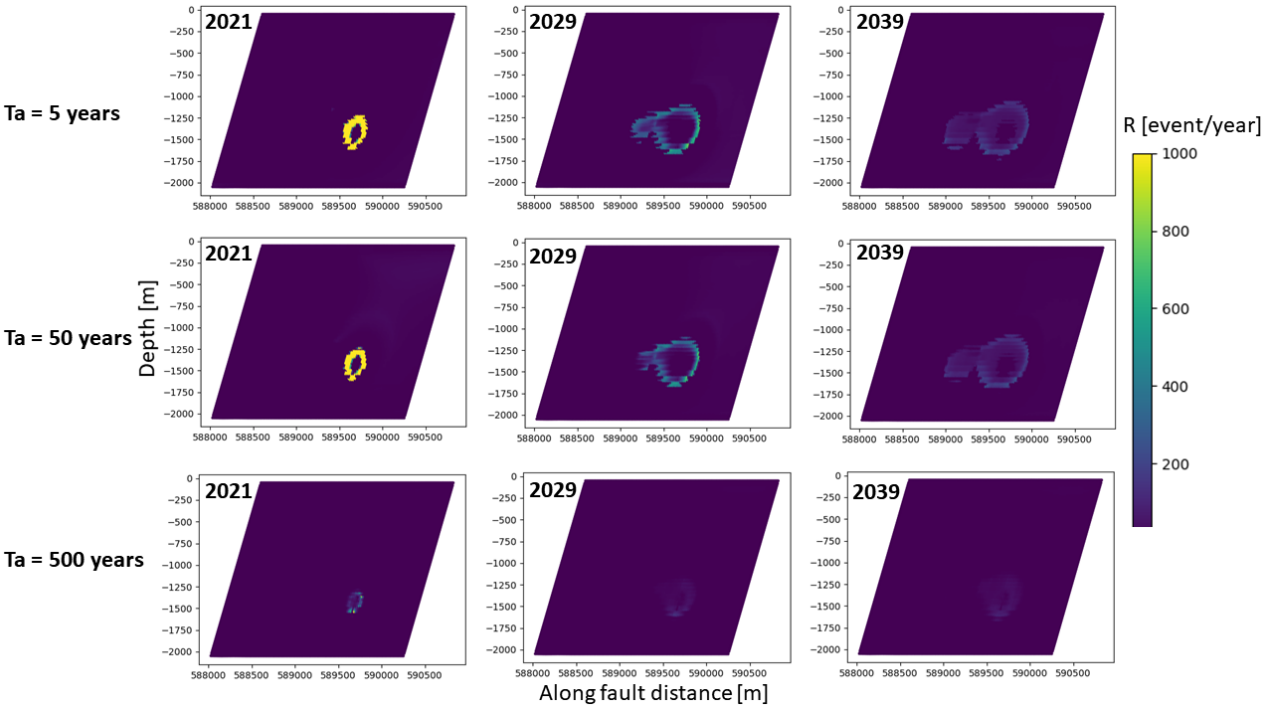

Figure 5-9. Strike-slip fault model: spatio-temporal evolution of relative seismicity rate R.

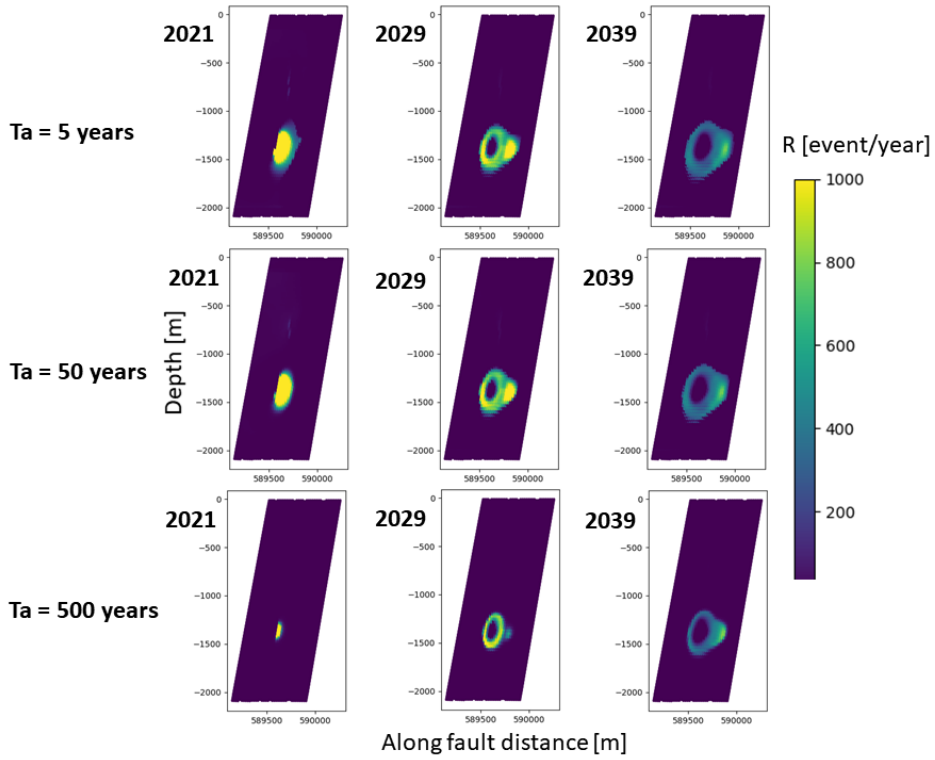

Figure 5-10. Normal-slip fault model: spatio-temporal evolution of relative seismicity rate R.

Dieterich's seismicity rate theory gives information about the nucleation rate of induced events, but no information in terms of their size. Once an event nucleates as predicted by Dieterich's seismicity rate theory, one can consider two end-members:

1 The rupture event can propagate all the way along the pre-existing fault surface.
2 The rupture event will stop at the margin of the perturbed zone (zone where the Coulomb stress have been levelled up by the pressure/temperature changes) before reaching the fault edges.

The first end-member assumes the Coulomb stresses before the start of circulation-production are already high and close to the failure threshold. Consequently, any induced events can potentially propagate all the way along the pre-existing fault surface. The second end-member assumes the initial level of Coulomb stresses to be relatively low when compared to the failure threshold. Consequently, when an induced event nucleates, it will only propagate inside the perturbed zone, that is the zone along the fault plane where the Coulomb stress have been increased due to the changes in pressure and temperature.

For the first end-member, the rate of occurrence of magnitude Mw earthquakes can be computed as the product of two factors (i) the rate of nucleation (given by the Dieterich's seismicity rate theory), and (ii) the probability that the nucleation occurs on a fault segment with a size which can yield a magnitude Mw event considering a typical static stress drop, that is the Gutenberg-Richter distribution. For the second end-member of low initial Coulomb stress level, these two factors need to be further multiplied by the probability of the fault segment to be entirely (or partially) confined inside the perturbed zone (see Maurer and Segall, 2018).

In our analysis we only consider the first end-member, thus assuming a relatively high initial level of Coulomb stress before the start of circulation-production. Figure 5-11 and Figure 5-12 present examples of simulations where samples are drawn randomly from the combination of the total (surface integrated) seismicity rate and the Gutenberg-Richter distribution. Background seismicity rate, static stress drop, and b-

value are kept constant for each simulation, at respective values of 0.01 event/year, 3MPa, and 1.0. The maximum magnitude Mw is also kept constant at 4.5 for each simulation, a magnitude typical for the size of the pre-existing faults and the static stress drop picked.

The cumulative total number of events at each magnitude is significantly smaller for the strike-slip fault than for the normal-slip fault model. Further, for the strike-slip model, when using the long characteristic delay T_a=500 years, the reduction of the seismicity rate peak as mentioned previously (see Figure 5-8), translates into a drastic decrease of the cumulative total number of events at each magnitude. In line with what we observed previously for the seismicity rate (see Figure 5-8), the effect of T_a on the frequency magnitude distribution of the normal-slip fault model is much smaller.

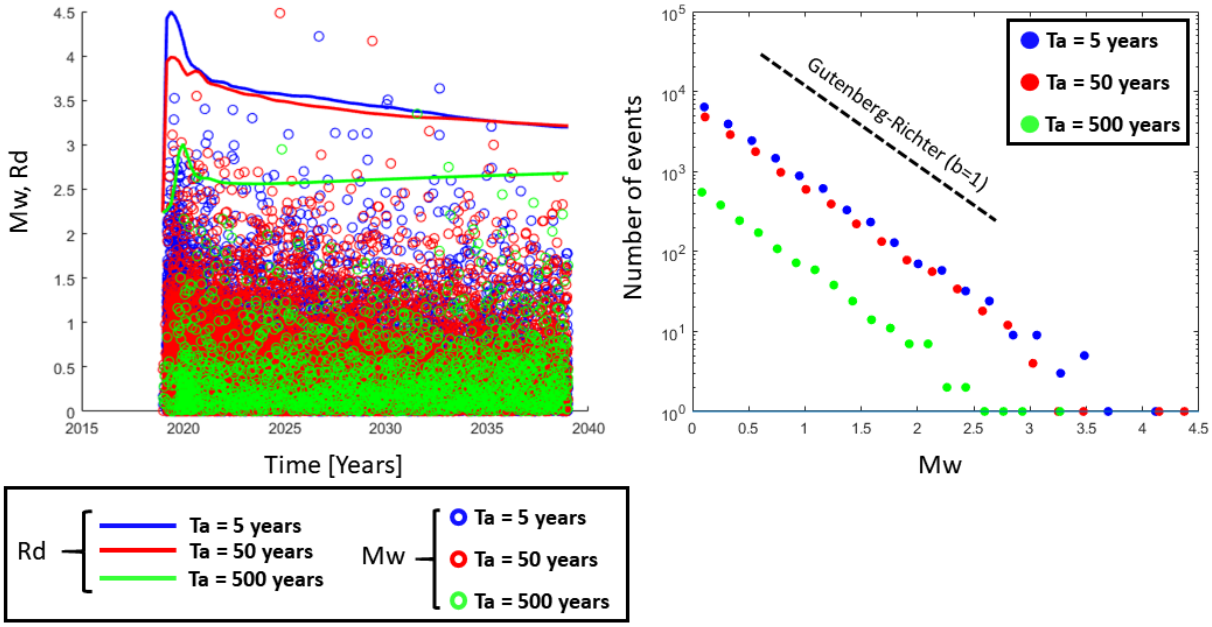

Figure 5-11. Strike-slip fault model: Example of simulations for induced events assuming a high initial Coulomb stress environment. Left: Magnitudes over time. The thick lines show the total (surface integrated) rates of events, log10(Rd). Right: Frequency magnitude distributions.

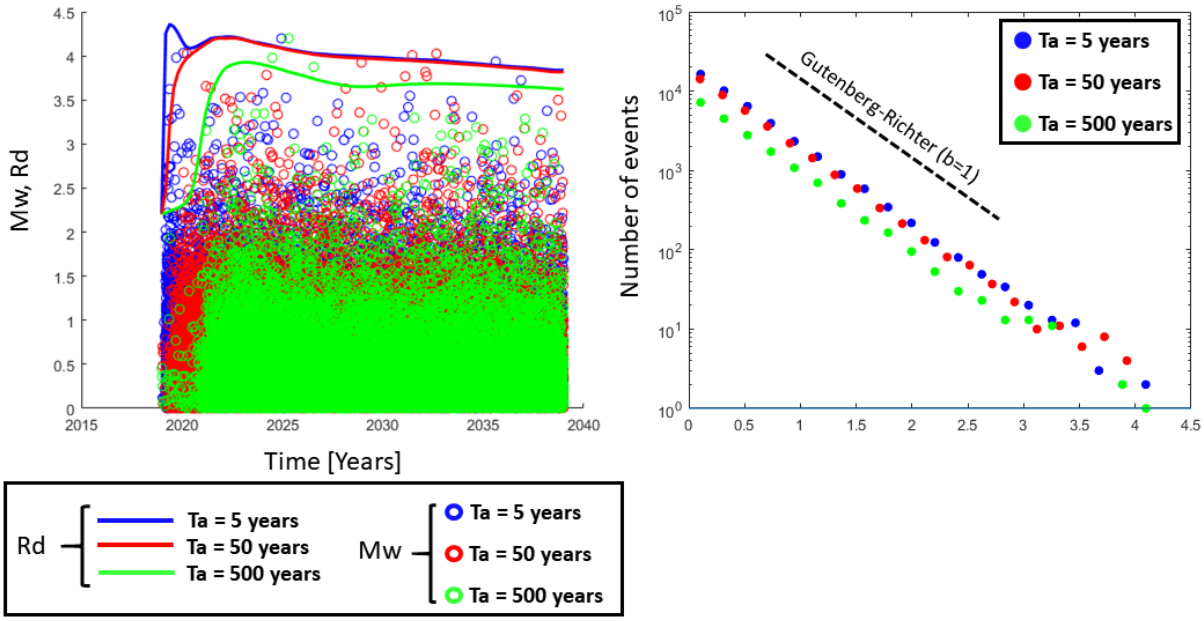

Figure 5-12. Normal-slip fault model: Example of simulations for induced events assuming a high initial Coulomb stress environment. Left: Magnitudes over time. The thick lines show the total (surface integrated) rates of events, log10(Rd). Right: Frequency magnitude distributions.

5.4 Discussion and Conclusions

We employed typical values for the model parameters in our analysis, both for modelling the stress and the seismicity. Consequently, our modelling results in terms of relative seismicity rate should be seen as an average expected behavior. We consider the modelled high relative rate of induced seismicity ($R>10^4$, see Figure 5-8) as representative and robust. However, in the absence of a long-term recording of seismicity data before circulation-production, it is difficult to constrain the background seismicity rate. Indeed, the preliminary analysis of the dataset during the short monitoring period (May 2018 to July 2019) indicates that only one event was recorded in the area of interest (Figueroa, 2019; Peters et al., 2020). Therefore, in our analysis the absolute rate of seismicity and thus the total cumulative number of events should be interpreted with caution. Still, when using a different background seismicity rate, the relative difference in terms of total cumulative number of events and frequency magnitude distribution between the strike-slip fault model and the normal-slip fault model remains the same.

The frequency-magnitude distributions have been derived assuming a high initial level of Coulomb stress along the pre-existing faults. Following this assumption, our rates of relatively large magnitude events are probably over-estimated since some of those might be arrested before reaching the edges of the fault. The extent of the faults is also not well constrained.

For both, the strike-slip fault model and normal-slip fault model, our analysis demonstrates that induced thermoelastic stress changes can lead to a high relative rate of induced seismicity ($R>10^4$, see Figure 5-8). The risk of induced seismicity by cooling of the pre-existing faults is thus expected to be high. Our analysis predicts a higher level of induced Coulomb stress and induced seismicity for the normal-slip fault model than for the strike-slip fault model. The number of events at each magnitude is expected to be higher for the normal-slip fault model than for the strike-slip fault model.

6 Conclusions

Based on the stimulation concepts from D7.2 (Hofmann et al., 2020), development scenarios were formulated to estimate the potential heat production that might be achieved from an EGS development at Acoculco. In total four different stimulation concepts were used: hydraulic fracture (tensile), stimulated fracture network, stimulated fault (zone), and a combination of stimulated fractures and faults. Each concept results in a different shape and size of the stimulated rock volume and was implemented at three different depths. The main uncertainty in the estimation of the heat production is the size, shape and permeability of the stimulated area. This uncertainty was included via the scenarios via a stochastic approach in which 50 realizations were simulated per scenario. The range in the stimulated rock volume spans three orders of magnitude and the produced heat ranges from less than 2 MW to 40 MW (downhole and averaged over 20 years of production). At this point in time, the information is insufficient to indicate which scenarios are most likely, and thus the results should be interpreted as indications rather than realistic estimates of the potential production.

The scenarios with a hydraulic fracture all suffered from premature thermal breakthrough and none of the scenarios produced more than 12 MW. The stimulated fault suffered from large pressure drawdown near the wells due to the small inflow zone into the well. The results of the scenarios show that none of the scenarios in which the stimulation affected the area just below the casing at 800 m depth produced more than 10 MW heat downhole. Also, the wellbore modelling showed that production to the surface was difficult for this depth. The scenarios at 1500 m and 1800 m depth with a stimulated fracture network or fault showed most promise and the best production characteristics. It should be noted, however, that the presence of a sufficiently dense and connected fracture network is speculation at this moment in time.

The analysis of induced seismicity demonstrates, for both the strike-slip fault model and normal-slip fault model, that induced thermoelastic stress changes can lead to a high relative rate of induced seismicity ($R>10^4$). Induced seismicity by cooling of the pre-existing faults is thus identified as a clear risk in this study. Our analysis predicts a higher level of induced Coulomb stress and associated induced seismicity for the normal-slip fault model than for the strike-slip fault model. The number of events at each magnitude is expected to be higher for the normal-slip fault model than for the strike-slip fault model.

7 Acknowledgements

This publication is part of a project that received funding by the European Union's Horizon 2020 research and innovation programme under grant agreement number 727550 and the Mexican Energy Sustainability Fund CONACYT-SENER, project 2015-04-268074.

We acknowledge the Comisión Federal de Electricidad (CFE) for kindly providing the data. We also acknowledge all our European and Mexican colleagues within GEMex for their help and collaboration.

The content of this report reflects only the authors' view. The Innovation and Networks Executive Agency (INEA) is not responsible for any use that may be made of the information it contains.

8 References

Audigane, P., J.-J. Royer, and H. Kaieda. 2002. Permeability characterization of the Soultz and Ogachi large-scale reservoir using induced microseismicity. Geophysics, 67(1), 204–211.

Aunzo, Z.P., G. Bjornsson and G.S. Bodvarsson, 1991. Wellbore models GWELL, GWNACL, and HOLA. LBL-31428. Berkeley, CAL.

Bär, K. and Weydt, L. (eds.) 2019. Comprehensive report on the rock and fluid samples and their physical properties in the Acoculco and Los Humeros regions. GEMex D6.1.

Bastesen, E. Walter Wheeler; Anita Torabi, Baptiste Lepillier, Andrea Brogi, Domenico Liotta, Victor Hugo Garduno, Oscar García Hernández, Emmanuel Olvera Garcia 2020. Geological structures and analogue permeability studies in Los Humeros and Acoculco geothermal system. Poster presented a the GEMex final conference, Feb 2020, Potsdam.

Blöcher, G., E. Peters, C. Kluge, N. Ilangovan, D. Bruhn, H. Nick, 2016. SURE D3.1 Report on Stimulation Technologies for Geothermal Reservoirs.

Bickel, J.A. and R.B. Bratvold, 2008. From Uncertainty Quantification to Decision Making in the Oil and Gas Industry. Energy Exploration & Exploitation 26(5), 311-325.

Bjornsson, G. and G.S. Bodvarsson, 1987. A Multi-feedzone wellbore simulator. LBL 23723. Berkeley, CAL.

Bogdanov I.I., Mourzenko, V.V., Thovert, J.-F. and Adler, P.M. (2003). Pressure drawdown well tests in fractured porous media. Wat. Resources Res. 39(1), doi:10.1029/2000WR000080.

Bonté, D., J. Limberger, E. Trumpy, G. Gola, J.D. van Wees, 2019. Regional resource assessment and geothermal models. GEMex Deliverable D3.4.

Buijze, L., L.van Bijsterveldt, H. Cremer, B. Jaarsma, B. Paap, H. Veldkamp, B. Wassing, J.-D. van Wees, G. van Yperen, J. ter Heege. 2019. Induced seismicity in geothermal systems: Occurrences worldwide and implications for the Netherlands. Proceedings EGC 2019, The Hague, Netherlands, 11-14 June 2019.

Calcagno, P., Genter, A., Huenges, E., Kaltschmitt, M., Karytsas, C., Kohl, T., Ledru, P., Manzella, A., Thorhallsson, S., and vanWees, J. D. (2010). The ENGINE Coordination Action (ENhanced Geothermal Innovative Network for Europe). In Proceedings World Geothermal Congress 2010 and Bali and Indonesia and 25-29 April 2010.

Calcagno, P., E. Trumpy, L.C. Gutiérrez-Negrín, D. Liotta, G. Gola, 2020. Report on the integrated geomodels of Los Humeros and Acoculco. GEMex deliverable D3.1.

Candela, T., Osinga, S., Ampuero, J. P., Wassing, B., Pluymaekers, M., Fokker, P. A., ... & Muntendam-Bos, A. G. (2019). Depletion-induced seismicity at the Groningen gas field: Coulomb rate-and-state models including differential compaction effect. Journal of Geophysical Research: Solid Earth, 124(7), 7081-7104.

Canet, C., Trillaud, F., Prol-Ledesma, R., González-Hernández, G., Peláez, B., Hernández-Cruz, B., and Sánchez-Córdova, M. M.: Thermal history of the Acoculco geothermal system, eastern Mexico: Insights from numerical modeling and radiocarbon dating, Journal of Volcanology and Geothermal Research, 305, 56-62, 2015.

Contini, M. (eds.) 2020. Report on results, concepts and surveys for public engagement. GEMex Deliverable D7.4.

Courson, D. L. and Cowan, G. R. (1980). Method of producing self-propping fluid-conductive fractures in rock. United States Patent 4220205.

Deb, P., D. Knapp, G. Marquart, C. Clauser, 2019. Report on the numerical reservoir model used for the simulation of the Acoculco reservoir in Mexico. GEMex Deliverable D6.2.

Dieterich, J., 1994. A constitutive law for rate of earthquake production and its application to earthquake clustering, J. geophys. Res., 99, 2601.

Doe, T., R. McLaren and W. Dershowitz. 2014. Discrete Fracture Network Simulations of Enhanced Geothermal Systems. PROCEEDINGS, Thirty-Ninth Workshop on Geothermal Reservoir Engineering Stanford University, Stanford, California, February 24-26, 2014. SGP-TR-202.

Evans, K.F., A. Zappone, T. Kraft, N. Deichmann, F. Moia. 2012. A survey of the induced seismic responses to fluid injection in geothermal and CO2 reservoirs in Europe. Geothermics 41, 30-54. 10.1016/j.geothermics.2011.08.002.

Figueroa, A., Perton, M., Calo, M. and V. Márquez. 2019. Reporte técnico con la revisión de la actividad sísmica natural y/o antropogénica detectada en Acoculco. Mexican GEMex Etapa6 PT5.2 Seismic.

Gama R., Martinez I., Cedillo F., Reporte litologico-estructural megascopico de los nucleos cortados en el pozo exploratorio Acoculco N.1 ubicado en la porcion Noroccidental del Estado de Puebla, CFE, Departmento de Exploracion report No. DEX-AC-015/95, 1995.

Gholizadeh Doonechaly, N., Rahman, S.S., Kotousov, A., 2013. A New Approach to Hydraulic Stimulation of Geothermal Reservoirs by Roughness Induced Fracture Opening, In Jeffrey, B. (ed.), Effective and Sustainable Hydraulic Fracturing, Commonwealth Scientific and Industrial Research Organisation, Australia, doi:10.5772/45724.

González Partida, E., 2019. Presentación de resultados del PT 6.2b: Caracterización del yacimiento de Acoculco. 5a Reunión técnica-administrativa GEMex. CIAC-UMSNH, Morelia, Mich., November 25-26, 2019

Grant, M.A. (2016). Physical performance indicators for hdr/egs projects. Geothermics, 63:2-4.

Gupta H. and S. Roy, 2007. Geothermal Energy An alternative resource for the 21st century. Elsevier Science, https://doi.org/10.1016/B978-0-444-52875-9.X5000-X.

Heidbach O., Rajabi M., Reiter K., Ziegler M., 2016. WSM Team, World stress map database release 2016.

Hofmann, H., G. Blöcher, N. Börsing, N. Maronde, N. Pastrik, G. Zimmermann, 2014: Potential for enhanced geothermal systems in low permeability limestones – stimulation strategies for the Western Malm karst (Bavaria). Geothermics 51 (2014) 351–367.

Hofmann, H., F. Parisio, B. Lepillier, T. Candela, E. Peters, M. Kruszewski, 2020. Report on optimised stimulation scenario for Acoculco. GEmex deliverable D7.2.

Jung, R. (2013). EGS - Goodbye or Back to the Future 95. In Jeffrey, R., editor, Effective and Sustainable Hydraulic Fracturing, chapter 5, pages 95-121. InTech.

Kruszewski, M., H. Hofmann, F. Gomez Alvarez, C. Bianco, A. Jimenez Haro, V. Hugo Garduño, D. Liotta, E. Trumpy, A. Brogi, W. Wheeler, E. Bastesen, F. Parisio, 2020 (in review). Integrated Stress Field Estimation and Implications for Enhanced Geothermal System Development in Acoculco, Mexico. Submitted to *Geothermics*.

Lepillier, B., A. Daniilidis, N. Doonechaly Gholizadeh, P.-O. Bruna, J. Kummerow and D. Bruhn. 2019. Fracture flow permeability and stress dependency simulation applied to multi-reservoirs, multi-production scenarios analysis. Geothermal Energy, 7-24. doi.org/10.1186/s40517-019-0141-8

Liotta, D. and V.H. Garduño-Monroy (eds.), 2019. Final report on active systems: Los Humeros and Acoculco. GEMex Deliverable D4.1.

López-Hernández, A., García-Estrada, G., Aguirre-Díaz, G., González-Partida, E., Palma-Guzmán, H. and Quijano-Léon, J.: Hydrothermal activity in the Tulancingo-Acoculco Caldera Complex, central Mexico: Exploratory studies, Geothermics, 38, 279-293, doi: 10.1016/j.geothermics.2009.05.001, 2009.

Lorenzo Pulido, C., Flores Armenta, M., Ramírez Silva, G., 2010. Characterization of the Acoculco Geothermal Zone as HDR System. *GRC Transactions, 34 (2010).*

Maurer, J., & Segall, P. (2018). Magnitudes of Induced Earthquakes in Low-Stress EnvironmentsMagnitudes of Induced Earthquakes in Low-Stress Environments. Bulletin of the Seismological Society of America, 108(3A), 1087-1106.

Miskimins, J. (eds) 2019. Hydraulic Fracturing: Fundamentals and Advancements. SPE monograph series.

McClure, M.W. and R.N. Horne, 2014. An investigation of stimulation mechanisms in Enhanced Geothermal Systems. Int. J. of Rock Mechanics and Mining Sciences 72, 242-260. https://doi.org/10.1016/j.ijrmms.2014.07.011

Olasolo, P., M.C. Juárez, M.P. Morales, S. D´Amico and I.A. Liarte, 2016. Enhanced geothermal systems (EGS): A review. Renewable and Sustainable Energy Reviews 56, p. 133–144. http://dx.doi.org/10.1016/j.rser.2015.11.031.

Peters, E., M. Angelone, G. Bongiovanni, F. Spaziani, V. Verrubbi, M. Guidarelli, E. Priolo, T. Candela, J. D. van Wees, 2020. Report on environmental risk assessment and mitigation strategies. GEMex Deliverable D7.3.

Quinao, J.J.D. and S.J. Zarrouk, 2018. Geothermal resource assessment using Experimental Design and response surface, The Ngatamariki geothermal field, New Zealand. Renewable Energy 116A, 324-334.

Sanyal, S. K. (2010). On minimizing the levelized cost of electric power from enhanced geothermal systems. In Proceedings World Geothermal Congress 2010, Bali, Indonesia, 25- 29 April.

Schlumberger, 2018. Reference Manual ECLIPSE ®, version 2018.1. Schlumberger,

Segall, P. and Lu, S., 2015. Injection-induced seismicity: poroelastic and earthquake nucleation effects, J. geophys. Res.: Solid Earth, 120, 5082–5103.

Swyer, M.W., M. E. Uddenberg, T. T. Cladouhos, A. N. Steely, C. Forson and N. C. Davatzes, 2018. Preliminary Geothermal Resource Assessment of the St. Helens Seismic Zone Using the Results from the Geothermal Play-Fairway Analysis of Washington State Prospects. PROCEEDINGS, 43rd Workshop on Geothermal Reservoir Engineering Stanford University, Stanford, California, February 12-14, 2018. SGP-TR-213

Vogt C., Marquart, G., Kosack, C., Wolf, A., Clauser, C., 2012. Estimating the permeability distribution and its uncertainty at the EGS demonstration reservoir Soultz-sous-Forêts using the ensemble Kalman filter, *Water Resources Research, 48,* W08517, doi: 10.1029/2011WR011673.

Wees, J.D. van, M. Pluymaekers, S. Osinga, P. Fokker, K. van Thienen-Visser, B. Orlic, B. Wassing, D. Hegen and T. Candela, 2019. 3-D mechanical analysis of complex reservoirs: a novel mesh-free approach. Geophys. J. Int. (2019) 219, 1118–1130. doi: 10.1093/gji/ggz352.

Weydt, L. M., Ramírez-Guzmán, A. A., Pola, A., Lepillier, B., Kummerow, J., Mandrone, G., Comina, C., Deb, P., Norini, G., Gonzalez-Partida, E., Avellán, D. R., Macías, J. L. , Bär, K., and Sass, I.: Petrophysical and mechanical rock property database of the Los Humeros and Acoculco geothermal fields (Mexico), Earth System Science Data, (2020, submitted).

Weydt, L. M., Bär, K., Colombero, C., Comina, C., Deb, P., Lepillier, B., Mandrone, G., Milsch, H., Rochelle, C. A., Vagnon, F., and Sass, I.: Outcrop analogue study to determine reservoir properties of the Los Humeros and Acoculco geothermal fields, Mexico, Adv. Geosci., 45, 281-287, https://doi.org/10.5194/adgeo-45-281-2018, 2018.

Wheeler, W., E. Bastesen, D. Liotta, A. Brogi, V.H. Garduño Monroy, A. Jiminez Haro, Fi. Gómez and E. González Partida, 2020. Fault models of the Acoculco borehole area for 3D architecture and fluid flow appraisal. Presented at the GEMex final conference, Potsdam, Feb 2020.

Witter et al 2019: Uncertainty and risk evaluation during the exploration stage of geothermal development: A review. Geothermics78, 233-242. doi.org/10.1016/j.geothermics.2018.12.011.

Zimmermann, G., Moeck, I., and Blöcher, G. (2010). Cyclic waterfrac stimulation to develop an Enhanced Geothermal System (EGS) - Conceptual design and experimental results. Geothermics, 39(1):59-69.

Coordination Office, GEMex project

Helmholtz-Zentrum Potsdam
Deutsches GeoForschungsZentrum

Telegrafenberg, 14473 Potsdam

Germany